Morphology of radio relics – II. Properties of polarized emission

P. Domínguez-Fernández [1,2]★ M. Brüggen,[1] F. Vazza [1,3,4] M. Hoeft,[5] W. E. Banda-Barragán,[1]
K. Rajpurohit [3,4] D. Wittor,[1] A. Mignone,[6] D. Mukherjee [7] and B. Vaidya [8]

[1]*Hamburger Sternwarte, Universität Hamburg, Gojenbergsweg 112, D-21029 Hamburg, Germany*
[2]*Department of Physics, School of Natural Sciences UNIST, Ulsan 44919, Republic of Korea*
[3]*Dipartimento di Fisica e Astronomia, Universitá di Bologna, Via Gobetti 92/3, I-40121, Bologna, Italy*
[4]*Istituto di Radio Astronomia, INAF, Via Gobetti 101, I-40121 Bologna, Italy*
[5]*Thüringer Landessternwarte (TLS), Sternwarte 5, 07778 Tautenburg, Germany*
[6]*Dipartimento di Fisica, Università di Torino, via Pietro Giuria 1, I-10125 Torino, Italy*
[7]*Inter-University Centre for Astronomy and Astrophysics, Post Bag 4, Pune - 411007, India*
[8]*Discipline of Astronomy, Astrophysics and Space Engineering, Indian Institute of Technology Indore, Khandwa Road, Simrol, Indore 453552, India*

ABSTRACT
Radio relics are diffuse radio sources in galaxy clusters that are associated with merger shock waves. Detailed observations of radio relics in total intensity and in polarization show complex structures on kiloparsec scales. The relation between the observed features and the underlying morphology of the magnetic field is not clear. Using 3D magneto-hydrodynamical simulations, we study the polarized emission produced by a shock wave that propagates through a turbulent medium that resembles the intracluster medium. We model the polarized synchrotron emission on the basis of diffusive shock acceleration of cosmic ray electrons. We find that the synchrotron emission produced in a shocked turbulent medium can reproduce some of the observed features in radio relics. Shock compression can give rise to a high polarization fraction at the shock front and a partial alignment of the polarization *E*-vectors with the shock normal. Our work confirms that radio relics can also be formed in an environment with a tangled magnetic field. We also discuss the effect of Faraday rotation intrinsic to the source, and how our results depend on the angular resolution of observations.

Key words: acceleration of particles – MHD – shock waves – methods: numerical – galaxies: clusters: intracluster medium – intergalactic medium.

1 INTRODUCTION

Radio observations of galaxy clusters reveal Mpc-scale diffuse emission in the intracluster medium (ICM). *Radio relics* are located at the cluster periphery, with elongated shapes and typically large degrees of polarization (see Brüggen et al. 2012; van Weeren et al. 2019 for reviews). Recent high-resolution radio observations have shown that radio relics have a complex morphology on smaller scales, consisting of filaments, bristles, and other substructures that cannot be classified in a single group (e.g. Owen et al. 2014; van Weeren et al. 2017; Di Gennaro et al. 2018; Rajpurohit et al. 2018, 2020a, 2021a; Botteon et al. 2020b).

Radio relics are believed to trace shock waves generated during mergers of galaxy clusters (see Ensslin et al. 1998; Hoeft & Brüggen 2007; van Weeren et al. 2011a; Nuza et al. 2017; Brüggen & Vazza 2020 or Bykov et al. 2019 for a review). For those relics that do not resemble merger shocks, it has been suggested that they have their origin in bubbles of relativistic electrons injected by jets from active galaxy nuclei (AGN) that will be re-energized upon a shock passage (e.g. ZuHone et al. 2020). One plausible mechanism that accelerates synchrotron-emitting cosmic ray electrons (CRe) in shocks is the

diffusive shock acceleration (DSA; e.g. Blandford & Eichler 1987; Drury 1983). Nevertheless, only a few radio relics can be explained exclusively by DSA of electrons from the thermal pool (e.g. Locatelli et al. 2020). In most cases, the radio power is too large to be explained by DSA of electrons from the thermal pool (see van Weeren et al. 2019; Botteon et al. 2020a). An alternative model is that a pre-existing population of mildly relativistic CRe ($10 \lesssim \gamma \lesssim 10^4$) exists (e.g. Kang, Ryu & Jones 2012; Pinzke, Oh & Pfrommer 2013) that gets re-accelerated by the DSA mechanism. This population of pre-existing CRe could potentially be injected by AGN.

The observed polarization fraction in several radio relics is inferred to be locally up to 65 per cent (e.g. van Weeren et al. 2010, 2012; Owen et al. 2014; Kierdorf et al. 2017; Loi et al. 2020; Rajpurohit et al. 2020b). It is often observed that the polarization electric field vector (*E*-vector) is aligned with the shock normal, i.e. the polarized magnetic field vector (*B*-vector) is aligned with the shock front (e.g. Bonafede et al. 2009a, b; van Weeren et al. 2010; Golovich et al. 2017; Pearce et al. 2017). Other observations of radio relics show similar trends even though one should note that in some cases the *E*-vectors are not corrected for Faraday rotation (e.g. Kale et al. 2012; de Gasperin et al. 2014, 2015). A compilation of polarized radio relics can be found in table 1 of Wittor et al. (2019). The alignment could either be produced by a large-scale uniform or compression of a randomly oriented magnetic field (e.g. Laing 1980; Ensslin

★ E-mail: pdominguez@hs.uni-hamburg.de

et al. 1998). It is also not clear whether the typically observed mild strength of shocks ($\mathcal{M}_{radio}{}^1 \sim 1.7$–4.6) would be enough to explain this alignment (e.g. Clarke & Ensslin 2006; van Weeren et al. 2010, 2012). Furthermore, the observed degree of alignment in relics might also depend on the viewing angle if the polarization is caused by compression of a small-scale tangled magnetic field. In particular, a relic viewed face-on is expected to have a less coherent alignment than the edge-on view (e.g. Skillman et al. 2013; Wittor et al. 2019). This happens because only the perpendicular components of the magnetic field with respect of the shock's normal are affected by the shock, while the parallel component is conserved. On the other hand, the observed degree of alignment and polarization would not depend on the viewing angle if the observed region of the ICM underlines a large-scale homogeneous uniform magnetic field.

The high polarization fraction, particularly at high radio frequencies, in radio relics makes them ideal objects for studying magnetic field properties of the ICM. However, modelling the observed features of radio relics is challenging from a numerical point of view. On one hand, cosmological simulations lack the resolution to solve the CRe's cooling scales (e.g. Skillman et al. 2013; Hong, Kang & Ryu 2015; Nuza et al. 2017; Wittor et al. 2019). On the other hand, particle-in-cell (PIC) simulations can only tell us about the dynamics at microphysical scales (e.g. Caprioli & Spitkovsky 2014a, b; Guo, Sironi & Narayan 2014; Park, Caprioli & Spitkovsky 2015; Ryu, Kang & Ha 2019; Kang, Ryu & Ha 2019). Therefore, it is relevant to bridge the gap of spatial scales between PIC and cosmological simulations. In Paper I, we modelled the synchrotron emission in a small fraction of the ICM by means of a new hybrid particle and fluid framework using the magneto-hydrodynamical (MHD) code PLUTO (Mignone et al. 2007; Vaidya et al. 2018). This method uses *Lagrangian* particles, each with its individual energy spectrum, embedded in a large-scale MHD simulation.

In Paper I, we studied a set-up where a shock was launched in an initially turbulent ICM. We studied how the properties of the upstream ICM are related to the synchrotron properties of radio relics assuming DSA. Some of the main results of Paper I are:

(i) The existence of complex substructure in the radio maps is a result of turbulence in the ICM.

(ii) The interaction of a shock with a turbulent medium can reproduce the discrepancy between Mach numbers as inferred from X-ray and radio emission. We found that one cause of this discrepancy is the stronger dependence of the synchrotron emission on the compression in the shock and therefore the higher Mach numbers in the tail of the Mach number distribution. We also found that the amplitude of the magnetic field fluctuations decreases more slowly than the density and temperature fluctuations, which adds to the observed Mach number discrepancy.

(iii) The magnetic power spectrum of a decaying turbulent medium remains largely unaffected at $\lesssim 10$ kpc scales by shocks with typical sonic Mach numbers of $\mathcal{M} = 2$–3. Independently of the initial type of turbulence, we found that shock compression and propagation shift the magnetic power spectra towards higher wave numbers (smaller scales) initially, and afterwards it generates post-shock turbulence leading to a shift of the turbulent power towards smaller wave numbers (larger scales).

(iv) $\mathcal{M} = 2$ shocks are not strong enough to modify the initial pre-shock magnetic field. This implies having an unrealistically high acceleration efficiency.

$^1\mathcal{M}_{radio}$ is the Mach number inferred from radio observations.
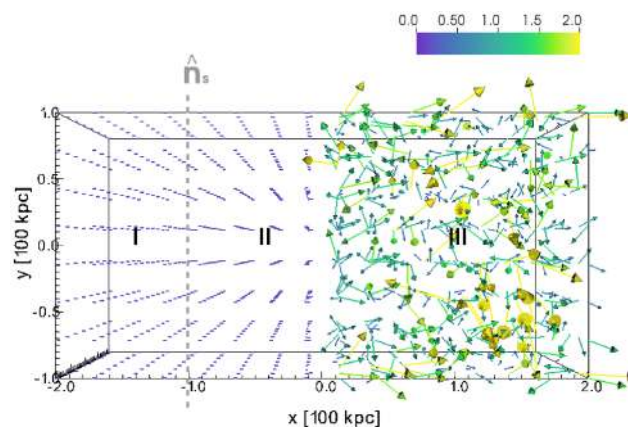
Figure 1. Initial magnetic field configuration in the PLUTO code. The vectors are coloured according to the magnitude of the magnetic field as shown in the upper colour bar in units of μG. I denotes the post-shock region, II denotes the uniform pre-shock region, and III the turbulent pre-shock region. The left side is a uniform medium with a B_x component matching the mean value of the B_x of the turbulent medium. We have one Lagrangian particle per cell placed in the whole regions II and III. The dashed grey line denotes the location of the shock discontinuity.

In this work, we extend our study of Paper I by including the modelling of polarized emission. Our aim is to study how the structure of the radio emission that is now observed in various radio relics would be observed in polarization. A recent high-resolution and high-sensitivity polarimetry study of the cluster CIZA J2242.8+5301 (e.g. Di Gennaro et al. 2021) indicates that the polarization emission can decrease towards the downstream. We expect that other highly resolved relics such as the Toothbrush relic in the galaxy cluster 1RXS J0603+4214 (e.g. Rajpurohit et al. 2018) or the MACS J0717.5+3745 relic (e.g. Bonafede et al. 2009b; Rajpurohit et al. 2021a) would give us also more information about the downstream characteristics of relics when observed in polarization.

We consider the same set-up as in Paper I, i.e. we drive a shock through a turbulent medium that is representative of a small region of the ICM. We then assume that CRe are injected instantly at the shock discontinuity and acquire an initial energy distribution based on DSA. The paper is structured as follows: in Section 2, we describe our numerical set-up and initial conditions. In Section 3, we include a description of the polarized emissivity and explain how we obtain the Stokes U and Q parameters maps. Section 4 shows our results for a uniform and a turbulent ICM and finally, we summarize in Section 5. Throughout this paper, we assume a ΛCDM cosmology (e.g. Aghanim et al. 2020).

2 NUMERICAL SET-UP

The basic set-up of our simulation is the same as in Paper I. Our computational domain is a rectangular box (400 kpc × 200 kpc × 200 kpc with 256 × 128 × 128 cells, respectively), where $x \in [-200,200]$ kpc, $y \in [-100,100]$ kpc, and $z \in [-100,100]$ kpc. The right half of the domain is filled with a turbulent medium representing a realistic ICM. The left half contains a uniform pre- and post-shock medium, between which a shock is launched. We define a shock discontinuity at $x = -100$ kpc (see Fig. 1 for the initial configuration of the magnetic field). This defines three regions in our simulation box: a post-shock uniform region (I), a pre-shock uniform region (II), and a pre-shock turbulent region (III; see Fig. 1 and section 2.2 in Paper I).
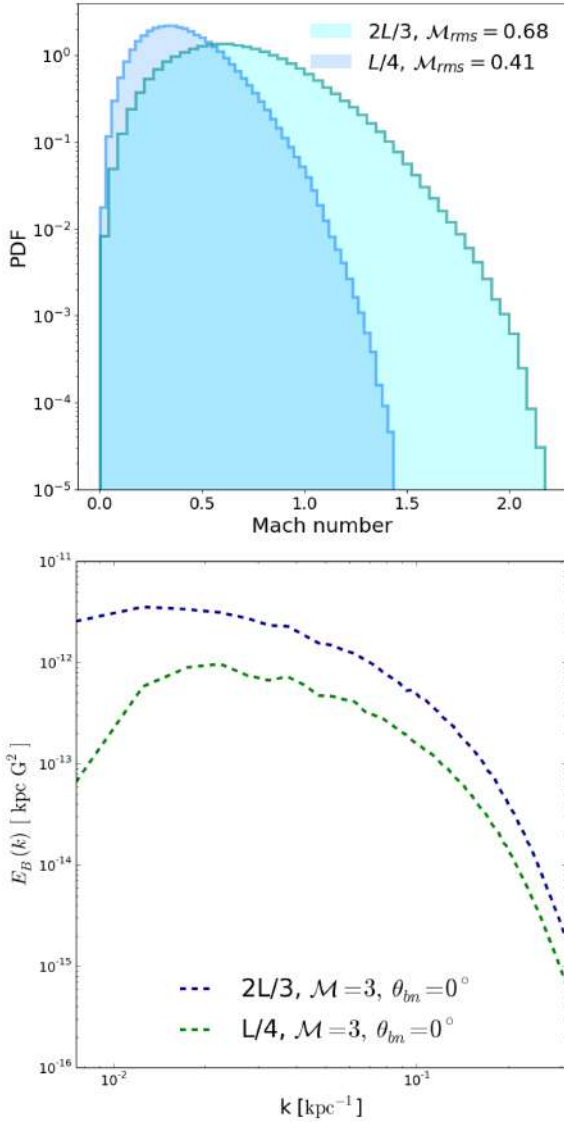
Figure 2. *Upper panel*: Initial distribution of Mach numbers in the 2*L*/3 and *L*/4 turbulent media. *Lower panel*: Initial magnetic power spectra of the 2*L*/3 and *L*/4 turbulent media.

The turbulent ICM initial conditions for region (III) were produced using the MHD FLASH code, version 4.6.1 (Fryxell et al. 2000; Calder et al. 2002). Each initial condition is self-consistently turbulent, i.e. the density, velocity, temperature, and magnetic field are turbulent fields. We produced two different turbulent media whose main characteristics are summarized as:[2]

(i) 2*L*/3 *turbulent medium*: Power peaks in 2/3 of the 200 kpc box, representing an injection scale of 133 kpc. Plasma-beta of ∼110 and an rms sonic Mach number of $\mathcal{M}_{rms} \sim 0.68$ (see Fig. 2). This medium has a mean density of 0.8×10^{-3} cm^{-3} and a mean magnetic field of 1 μG.

(ii) *L*/4 *turbulent medium*: Power peaks in 1/4 of the 200 kpc box, representing an injection scale of 50 kpc. Plasma-β of ∼110 and an rms sonic Mach number of $\mathcal{M}_{rms} \sim 0.41$ (see Fig. 2). This medium

[2]For all specifics regarding these FLASH simulations we refer the reader to section 2.1 in Paper I.

has a mean density of 0.8×10^{-3} cm^{-3} and a mean magnetic field of 1.5 μG, where the plasma-β is defined as the ratio of the plasma pressure to the magnetic pressure, $\beta = 8\pi P/B^2$. The rms Mach number $\mathcal{M}_{rms}$ is an integral quantity defined as $(\int v^2 \mathrm{d}V / \int c_s^2 \mathrm{d}V)^{1/2}$, where v is the velocity field, c_s is the sound speed, and V is the volume of the computational domain. In the lower panel of Fig. 2, we show the magnetic power spectra of both initial conditions in which the injection scale or peak spectra is better visualized.

We used the ideal MHD code PLUTO (Mignone et al. 2007) to evolve this system in the presence of shock acceleration and then compute the polarized emission. We assumed an ideal equation of state that is an adiabatic index $\gamma_0 = 5/3$. The initial boundary conditions of the computational domain are *outflow* in x (zero gradient across the boundary) and *periodic* in y and z. We used a piece-wise parabolic method for the spatial integration, whereas a second order TVD Runge–Kutta method for the time stepping with a Courant–Friedrichs–Lewy condition of 0.3. The Riemann solver for the flux computation that we used is the Harten–Lax–van Leer discontinuities solver (see Miyoshi & Kusano 2005). We control the $\nabla \cdot \mathbf{B} = 0$ condition with the hyperbolic divergence cleaning technique where the induction equation is coupled to a generalized Lagrange multiplier (GLM; e.g. Dedner et al. 2002).

We performed simulations with both turbulent media from Paper I, namely the 2*L*/3 and *L*/4 cases. The initial conditions for the density, pressure, and velocity in region II (*pre-shock* uniform region at [−100,0] kpc) are set to the mean value of the corresponding turbulent fields. In the case of the magnetic field in region II, we set it to be the mean value of the B_x component of the turbulent medium. The initial conditions for region I (*post-shock* region) are selected according to the MHD Rankine–Hugoniot conditions (e.g. Landau & Lifshitz 1987). We set up an initial shock with sonic Mach number $\mathcal{M}$ and study the polarization as observed from different lines of sight (LOS) and frequencies. Finally, we fill the computational domain from the shock discontinuity up to the right side of the box with one *Lagrangian* particle per cell. This gives us a total number of 3 145 728 Lagrangian particles for each run. Each particle evolves according to the following prescription:

(i) *Activation*: Each Lagrangian particle is activated once it is located in a shocked cell (see section 3.1 and appendix B in Paper I for a description of the activation and the shock finder algorithm). At that moment, the particle acquires an energy spectrum according to DSA theory (see section 3.1 in Paper I). We assumed a fixed acceleration efficiency of $\eta = 10^{-3}$ and fixed energy limits of $\gamma_{min} = 1$ and $\gamma_{max} = 10^5$ (energy high enough to model observations at 6.5 GHz in a ∼ 1 μG magnetic field region). The final synchrotron emission can be re-scaled to other values of η since in our case the energy limits remain constant and the accelerated CRe do not have any feedback on the shock evolution. We defer to future work a more extensive study on the role of different model choices for η and γ_{min} (which are poorly constrained in the DSA theory of cosmic ray electron acceleration; see Malkov & Drury 2001 and references therein for a general review on DSA at collisionless shocks and its challenges).

(ii) *Evolution*: The energy spectra of the particles evolve according to a cosmic ray transport equation involving adiabatic, synchrotron, and inverse Compton losses (see Vaidya et al. 2018).

All the parameters of our runs are summarized in Table 1. Shocks can be classified as quasi-parallel and quasi-perpendicular if $\theta_{bn} \leq 45°$ or $\theta_{bn} > 45°$, respectively, where θ_{bn} refers to the angle of the upstream magnetic field with respect to the shock normal. In this

Table 1. Initial conditions of region II: uniform pre-shock region ([−100,0] kpc for the turbulent medium and [−100,200] for the uniform medium). The initial conditions for the left side of the shock (region I) depend on the pre-shock conditions (region II) and the initial Mach number of the shock $\mathcal{M}$ through the Rankine–Hugoniot jump conditions. L denotes the length of the turbulent region, i.e. 200 kpc. θ_{bn} is the angle of the upstream magnetic field with respect to the normal of the shock. Note that the magnetic field in region II has only an x-component, $B_{x,\,II}$, in the turbulent media. The two runs with turbulent media correspond to the IDs k1p5_M3_parallel and k4_M3_parallel in table 1 in Domínguez-Fernández et al. (2021; hereafter Paper I).

Uniform medium	$\mathcal{M}$	$\theta_{bn}[°]$	$\rho_{II}\,[10^{-27}\,\mathrm{g\,cm^{-3}}]$	$B_{II}\,[\mu G]$
1	3.0	0	1.34	0.4
2	3.0	90	1.34	0.4
Turbulent medium	$\mathcal{M}$	$\theta_{bn}[°]$	$\rho_{II}\,[10^{-27}\,\mathrm{g\,cm^{-3}}]$	$B_{II}\,[\mu G]$
2L/3	3.0	0	1.34	0.4
L/4	3.0	0	1.34	0.4

work, we consider for simplicity only two limits, i.e. $\theta_{bn} = 0°$ and $\theta_{bn} = 90°$ for the initially uniform medium and $\theta_{bn} = 0°$ for the initially turbulent medium. In the case of the turbulent medium it should be stressed that the initial $\theta_{bn} = 0°$ refers only to the initial angle of the average upstream magnetic field defined in region II with respect to the shock normal. Note that the magnetic field in region II only has an *x*-component and its value is defined such that it matches the mean value of the B_x component of the turbulent medium (region III). As the shock propagates through region III, θ_{bn} changes from cell to cell depending on the local magnetic topology. Nevertheless, throughout the paper we will use the notation $\theta_{bn} = 0°$ as a reference to the initial configuration. We refer the reader to Paper I for a more detailed description of the initial set-up.

For each configuration in Table 1, we produced polarization maps at three frequencies: 150 MHz, 1.5 GHz, and 6.5 GHz. We restricted ourselves to consider only these configurations (see Table 1) because in Paper I we found that $\mathcal{M} = 2$ shocks in our set-up are unlikely to reproduce observable radio relics. In Paper I, we also found differences in the synchrotron emission computed with the two different turbulent media. Here we focus on the correspondent differences produced in the polarized emission. We also leave the cases with $\theta_{bn} = 90°$ out of this work as the study of the shock obliquity will be subject of our study in the third paper in this series.

3 POLARIZED EMISSION FROM SHOCKS

The linearly polarized emission is computed in a similar fashion as the synchrotron emission (see Ginzburg & Syrovatskii 1965):

$$\mathcal{J}'_{pol}(\nu'_{obs}, \hat{\mathbf{n}}'_{los}, \mathbf{B}') = \frac{\sqrt{3}e^3}{4\pi m_e c^2}|\mathbf{B}' \times \hat{\mathbf{n}}'_{los}| \int N(E')G(\xi)\,\mathrm{d}E', \quad (1)$$

where $\mathbf{B}'$ is the local magnetic field, $\hat{\mathbf{n}}'_{los}$ is the unit vector in the direction of the LOS in the comoving frame. Each Lagrangian particle (or macro-particle) that represents an ensemble of CR electrons is characterized by an energy distribution function, $N(E)$ (as defined in Paper I). The macro-particle's energy distribution function at the activation time is

$$\chi(E) = \frac{N(E)}{n_0} = \frac{N_0}{n_0}E^{-p}, \quad (2)$$

where $p = q − 2$ is the energy *injection spectral index*, q is the power-law index of the corresponding particle momentum distribution and related to the shock Mach number $\mathcal{M}$ via the DSA theory, N_0 is the normalization factor, and n_0 is the fluid number density (see

section 3.1 of Paper I). N_0 is assigned according to the kinetic energy contained in the shock. That is, we considered that the total energy per fluid number density is

$$\int \chi(E)\,E\,\mathrm{d}E = \frac{E_{tot}}{n_0}, \quad (3)$$

where $E_{tot} = \eta\,E_{shock} = \eta\,\frac{1}{2}\rho_{post}\,v_{shock}^2$ and η is the acceleration efficiency. From these, we finally obtain the normalization factor:

$$N_0 = \begin{cases} \dfrac{\eta\,E_{shock}\,(4 - q)}{\left[E_{max}^{4-q} - E_{min}^{4-q}\right]} & \text{if } q \neq 4 \\[2ex] \eta\,E_{shock}\log\left(\dfrac{E_{max}}{E_{min}}\right) & \text{if } q = 4 \end{cases}. \quad (4)$$

Finally, $G(\xi) = \xi K_{2/3}(\xi)$, where $K_{2/3}(\xi)$ is a modified Bessel function and

$$\xi = \frac{\nu'_{obs}}{\nu'_c} = \frac{4\pi m_e^3 c^5 \nu'_{obs}}{3e\,E'^2|\mathbf{B}' \times \hat{\mathbf{n}}'_{los}|}, \quad (5)$$

where ν'_{obs} and ν'_c are the observing and critical frequencies, respectively. The reader should note that here the primed quantities refer to the comoving frame, whereas standard notation refers to the observer's frame. Note also that only those particles with pitch angle coinciding with the angle between $\mathbf{B}'$ and $\hat{\mathbf{n}}'_{los}$ contribute to the emission along the LOS in equation (1).

The polarized emissivity in equation (1) is measured in the local comoving frame with the emission region. To obtain the emissivity in a fixed observer's frame, we have to apply a transformation,

$$\mathcal{J}_{pol}(\nu_{obs}, \hat{\mathbf{n}}_{los}, \mathbf{B}) = \mathcal{D}^2 \mathcal{J}'_{pol}(\nu'_{obs}, \hat{\mathbf{n}}'_{los}, \mathbf{B}'), \quad (6)$$

where $\mathcal{D}$ is a Doppler factor (see equation 21 in Paper I). The unit vectors in the direction of the line of sight in the comoving and observer's frame are related via

$$\hat{\mathbf{n}}'_{los} = \mathcal{D}\left[\hat{\mathbf{n}}_{los} + \left(\frac{\gamma^2}{\gamma + 1}\mathbf{v}\cdot\hat{\mathbf{n}}_{los} - \gamma\right)\mathbf{v}\right], \quad (7)$$

where γ is the Lorentz factor of the tracer particle and $\mathbf{v}$ is the velocity in the Eulerian grid at the position of the Lagrangian particle and scaled to the speed of light.
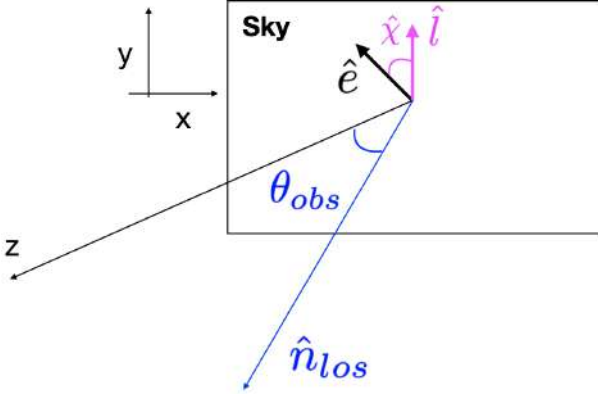
3.1 Polarization maps

In this work, we consider an observer's reference frame in which z lies along the LOS $\hat{\mathbf{n}}_{los}$ and x and y are in the plane of the sky. That is, we choose the vector $\hat{\mathbf{n}}_{los}$ according to an observing angle θ_{obs} with respect of the z-axis (see Fig. 3). The Stokes parameters Q and U maps can be obtained in the same fashion as the specific intensity (or surface brightness) maps by integrating along the LOS as

$$Q_\nu = \int \mathcal{J}_{pol}(\nu_{obs}, x, y, z)\cos 2\hat{\chi}\,\mathrm{d}z, \quad (8)$$

$$U_\nu = \int \mathcal{J}_{pol}(\nu_{obs}, x, y, z)\sin 2\hat{\chi}\,\mathrm{d}z, \quad (9)$$

where $\hat{\chi}$ is the local *polarization angle*, that is, the angle of the electric field vector in the plane of the sky measured from a unit vector also defined in the plane of the sky (see Section 3.2). This can be computed from the polarized emissivity $\mathcal{J}_{pol}$ that we have as a grid quantity, i.e. we assign the information given by the macro-particles back on to the Eulerian grid. The specific intensity (or surface brightness) maps can be obtained by integrating along a LOS as described in Paper I,

$$I_\nu = \int \mathcal{J}_{syn}(\nu_{obs}, x, y, z)\mathrm{d}z, \quad (10)$$

Figure 3. Schematic of the plane of the sky. The two polarizations on the plane of the sky are defined by the electric field unit vector $\hat{\mathbf{e}}$. The polarization angle $\hat{\chi}$ is then defined with respect of the unit vector $\hat{\mathbf{l}}$.

where $\mathcal{J}_{\text{syn}}$ is the synchrotron emissivity (section 3.2 in Paper I). Finally, equations (8)–(10) allow us to get the degree of (linear) polarization, or also referred as the *polarization fraction*,

$$\pi_\nu = \frac{\sqrt{Q_\nu^2 + U_\nu^2}}{I_\nu}. \tag{11}$$

3.2 The polarization angle

The PLUTO code computes the local polarization angle at each Lagrangian particle following the method described in Lyutikov, Pariev & Blandford (2003). The electric field unit vector of a linearly polarized electromagnetic wave in the comoving frame is normal to the local magnetic field unit vector, $\hat{\mathbf{B}}'$, and to the LOS, $\hat{\mathbf{n}}'_{\text{los}}$, i.e. directed along the unit vector $\hat{\mathbf{e}}' = \hat{\mathbf{n}}'_{\text{los}} \times \hat{\mathbf{B}}'$. In this way, the radiated magnetic field is therefore $\hat{\mathbf{b}}' = \hat{\mathbf{n}}'_{\text{los}} \times \hat{\mathbf{e}}'$. The electric field in the observer's frame obtained with Lorentz transformations is

$$\mathbf{e} = \gamma \left[\hat{\mathbf{e}}' - \frac{\gamma}{\gamma + 1}(\hat{\mathbf{e}}' \cdot \mathbf{v})\mathbf{v} - \mathbf{v} \times \hat{\mathbf{b}}' \right]. \tag{12}$$

On the other hand, the Lorentz transformation of Maxwell's equations in the ideal MHD case $\mathbf{E} + \mathbf{v} \times \mathbf{B} = 0$ allows us to express the comoving frame unit vector $\hat{\mathbf{B}}'$ in terms of the observer's frame unit vector $\hat{\mathbf{B}}$,

$$\hat{\mathbf{B}} = \frac{1}{\sqrt{1 - (\hat{\mathbf{B}}' \cdot \mathbf{v})^2}} \left[\hat{\mathbf{B}}' - \frac{\gamma}{\gamma + 1}(\hat{\mathbf{B}}' \cdot \mathbf{v})\mathbf{v} \right]. \tag{13}$$

Using equations (7) and (13), we obtain a general expression giving the polarization vector in terms of the observed quantities,

$$\hat{\mathbf{e}} = \frac{\hat{\mathbf{n}}_{\text{los}} \times \mathbf{q}}{\sqrt{q^2 - (\hat{\mathbf{n}}_{\text{los}} \cdot \mathbf{q})^2}}, \tag{14}$$

where

$$\mathbf{q} = \hat{\mathbf{B}} + \hat{\mathbf{n}}_{\text{los}} \times (\mathbf{v} \times \hat{\mathbf{B}}). \tag{15}$$

We can then introduce a unit vector $\hat{\mathbf{l}}$ normal to the plane containing $\hat{\mathbf{n}}_{\text{los}}$ (in our case it is defined in the y-axis of plane of the sky), and obtain the components of the $\mathbf{q}$ vector in the plane of the sky:

$$\cos \hat{\chi} = \hat{\mathbf{e}} \cdot (\hat{\mathbf{n}}_{\text{los}} \times \hat{\mathbf{l}}) \tag{16}$$

$$\sin \hat{\chi} = \hat{\mathbf{e}} \cdot \hat{\mathbf{l}}. \tag{17}$$

Equations (16) and (17) can be then rewritten in terms of $2\hat{\chi}$ using simple trigonometric relations and finally substituting in

equations (8) and (9). The plane of polarization suffers additional rotation as the radiation propagates through a magnetized medium, due to Faraday rotation. In order to take this (intrinsic) rotation into account, an additional contribution should be added to the observed polarization angle,

$$\hat{\chi} \longrightarrow \hat{\chi} + \text{RM}\, \lambda_{\text{obs}}^2, \tag{18}$$

where RM is the rotation measure defined as

$$\text{RM} = 0.812 \text{ rad m}^{-2} \int n_e B_\parallel \, \mathrm{d}l, \tag{19}$$

with the electron density n_e in units of 10^{-3} cm^{-3}, the component of the magnetic field parallel to the LOS $B_\parallel$ in μG and dl in pc. This means that when also considering the intrinsic Faraday rotation of the radio source, we substitute equation (18) into equations (8) and (9). We will study this effect in Section 4.3.

Note that while $\hat{\chi}$ defines the intrinsic angle at each point in the 3D simulation box, the polarization *E*–vector angle as measured by the observer is an integrated quantity that is computed using the Q and U Stokes maps:[3]

$$\psi = \frac{1}{2} \arctan\left(\frac{U_\nu}{Q_\nu} \right). \tag{20}$$

In the following we will use the ψ notation to refer to the polarization *E*-vector angle.

4 RESULTS

4.1 Uniform medium

To test our model, we start by presenting the polarization of a simple uniform medium. This means that the initial conditions for the pre-shock region (III) are equal to those in pre-shock region (II). We considered two orientations of the magnetic field (see 1 and 2 models in Table 1): in the x-direction parallel to the shock normal, i.e. $\theta_{\text{bn}} = 0°$, and in the y-direction perpendicular to the shock normal, i.e. $\theta_{\text{bn}} = 90°$. These runs will be used as control runs for comparison with the turbulent media presented in Section 4.2. We considered three different LOS defined by the observing angle, θ_{obs}: $0°, 45°, 60°$ (see Section 3).

The first case with a magnetic field in the plane of the sky (only an x-component) introduces simplifications such as $|\mathbf{B}' \times \hat{\mathbf{n}}'_{\text{los}}| \propto \cos(\theta_{\text{obs}})$ and $\cos \hat{\chi} = 0$. This also implies that the Stokes U_ν parameter is zero in equation (11) and that we can get estimates of the resulting Q_ν parameter and polarization degree Π_ν in terms of the values at $\theta_{\text{obs}} = 0°$:

$$Q_\nu(\theta_{\text{obs}}) \sim Q_\nu(0°) \cos^2(\theta_{\text{obs}}), \tag{21}$$

and therefore $\Pi_\nu(\theta_{\text{obs}}) \sim Q_\nu(0°)/I_\nu(0°)$. In Fig. 4, we show the I_{150} (top panel) and Q_{150} (bottom panel) profiles for a frequency of 150 MHz, at an epoch in which the shock front has reached almost the right end of the simulation box (≈ 178 Myr). We show the results for the observing angles $0°$, $45°$, and $60°$, respectively. The Stokes Q parameter should be then smaller than $Q(0°)$, by a factor of $\sim 1/2$ for the $45°$ observing angle and $\sim 1/4$ for the $60°$ observing angle (see equation 21), as shown in Fig. 4. Note that equations (8) and (9) are integrated along the z-axis, while the different LOS are defined through the observing angle between the LOS and the z-axis.

---

[3]The computation of arctan(θ) needs to consider the four quadrants, i.e. $\theta \in [-\pi, \pi]$
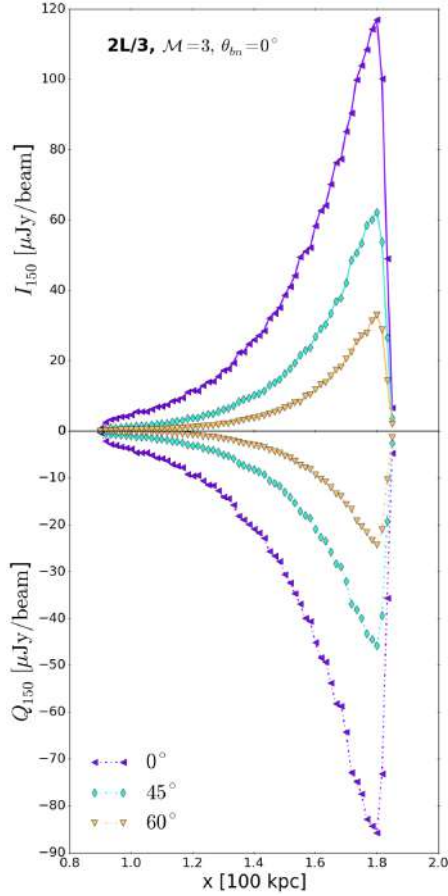
Figure 4. **Stokes I** parameter (or surface brightness) at 150 MHz (*top panel*) and **Stokes Q** parameter at 150 MHz (*bottom panel*) integrated along the *z*-axis at 178 Myr. We show the observing angles $\theta_{\rm obs} = 0°$, 45°, and 60° in purple, cyan, and yellow colours, respectively. We considered a beam of $\theta^2 = 5$ arcsec × 5 arcsec to get units of μJy per beam in order to have a LOFAR-HBA alike configuration. No smoothing is applied. Note that $\theta_{\rm obs}$ gives the angle between the local magnetic field and the LOS.

One of the major unknowns in the interpretation of real observed radio relics is the physical mechanism leading to the high degree of alignment of the magnetic field with the shock front. This can be tested in our simulations. We compute the polarization fraction with equation (11) and the polarization *E*-vector angle with equation (20).

In Fig. 5, we show polarization fraction maps along with the corresponding polarization *E*-vectors for the two alignments of the magnetic field, i.e. $\theta_{\rm bn} = 0°$ and $\theta_{\rm bn} = 90°$. We see a polarization fraction gradient towards the downstream region of the shock, i.e. the polarization fraction is lower at the shock front and it increases in the downstream region. The fractional polarization ranges from ∼0.7 to ∼0.8 for the two configurations. This is expected as the freshly activated particles at the shock front age moving downstream, which causes a steepening in their energy spectrum. The polarization fraction for an injection power-law E^{-p} is (e.g. Engel 1979; Rybicki & Lightman 1979)

$$\pi = \frac{p+1}{p+7/3}. \tag{22}$$

In our uniform runs, we have $p = 2.5$ (corresponding to $\mathcal{M} = 3$) corresponding to $\Pi = 0.724$ (see shock front values in Fig. 5). After activation the energy power-law index, p, increases due to synchrotron and inverse Compton losses. One can easily check that
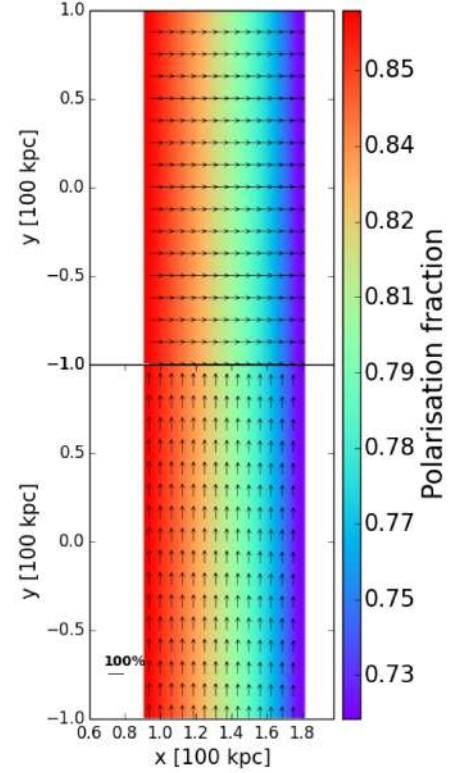

Figure 5. Polarization fraction for a uniform medium with a magnetic field oriented in the *y*-direction (*upper panel*) and the *x*-direction (*lower panel*). The polarization fraction computed with equation (11). We overplot the polarization *E*-vector computed with equation (20).

if p increases, Π increases as well, as shown in equation (22). In the $\theta_{\rm bn} = 0°$ case (see lower panel of Fig. 5), the polarization *E*-vectors are aligned with the shock surface (or *B*-vector is aligned with the shock normal), while in the $\theta_{\rm bn} = 90°$ case (see upper panel of Fig. 5), the polarization *E*-vectors are aligned with the shock normal as expected. The alignment of the polarization *E*-vectors with the shock normal is observed, for example, in the relic in MACS J1752.0+4440 (e.g. Bonafede et al. 2012), the relic in Abell 2744 (e.g. Pearce et al. 2017), the Sausage relic (van Weeren et al. 2010; Kierdorf et al. 2017; Loi et al. 2020; Di Gennaro et al. 2021), and the relic in ZwCl 0008.8+5215 (see van Weeren et al. 2011c; Golovich et al. 2017; Kierdorf et al. 2017). To summarize, in a uniform medium, we can obtain the same gradient in polarization for opposite alignments of the magnetic field with respect to the shock normal, i.e. $\theta_{\rm bn} = 0°$ and $\theta_{\rm bn} = 90°$.

4.2 Turbulent medium

An ICM with the level of uniformity presented in Section 4.1 is fairly unrealistic. Therefore, we proceeded to apply the same methods to study more realistic ICM conditions. We present 3D renderings of the polarized emission produced by our modelling for the 2*L*/3, $\mathcal{M} = 3$ and $\theta_{\rm bn} = 0°$ run in Fig. 6, as seen along the LOS defined by $\theta_{\rm obs} = 60°$ at 150 MHz. In the upper and lower panels of Fig. 6, we show the polarized emissivity corresponding to the Stokes Q and U parameters, respectively. The polarized emission is not spatially uniform and it coincides with the morphology of the synchrotron emissivity studied in Paper I. The combination of shock compression and turbulence produces fluctuations in the flow that are reflected into
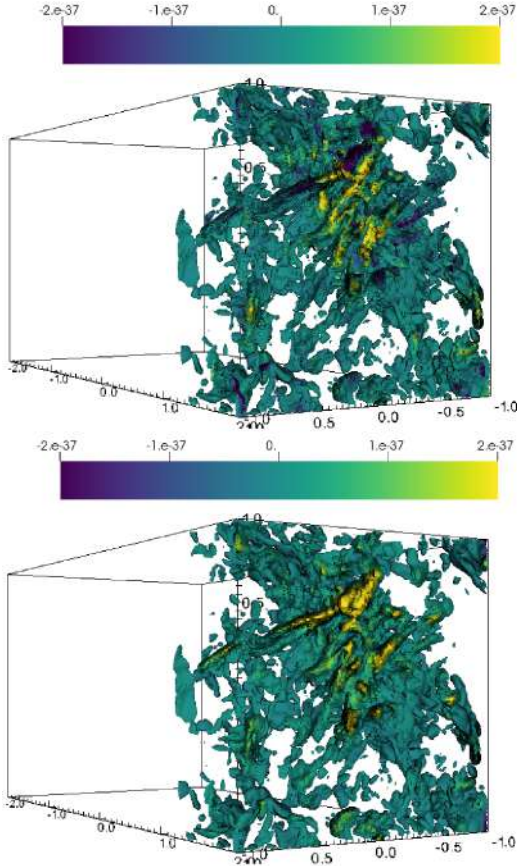
Figure 6. Visualization of the polarized emissivity $\mathcal{J}_{pol}$ isocurves for the $2L/3$, $\mathcal{M} = 3$ and $\theta_{bn} = 0°$ run at $t = 178$ Myr and at $\theta_{obs} = 60°$. The upper panel shows the polarization corresponding to the **Stokes Q** parameter (i.e. $\mathcal{J}_{pol} \cos 2\hat{\chi}$, see equation 8), while the lower panel shows its corresponding **Stokes U** parameter (i.e. $\mathcal{J}_{pol} \sin 2\hat{\chi}$, see equation 9) The emissivity is shown in units of [erg cm^{-3} s^{-1} Hz^{-1} str^{-1}]. The axes are shown in units of [100 kpc].

the shape of threads and filaments. These are visible in the total and polarized intensity maps. This fining is intriguing as it suggests that such physical configuration (i.e. a shock running over a turbulent ICM) can well explain recently observed radio structures in high-resolution maps of radio relics (e.g. Owen et al. 2014; van Weeren et al. 2017; Di Gennaro et al. 2018; Rajpurohit et al. 2018, 2020a, 2021a). The characteristic size of the synchrotron emissivity and the magnetic field were previously studied in Paper I. There we found that both are of the order of ~70–100 kpc, depending on the model (see fig. 18 in Paper I). Nevertheless, the size of single threads, bristles, and filaments in the synchrotron emissivity are not simply reflecting the shape of magnetic structures. The observed radio emission also depends on the particles' energy spectrum, which differs from location to location due to the different energy losses across the relic area. Likewise, the emissivity fluctuations may be even larger if the acceleration efficiency has a strong dependence on the local plasma conditions. It is possible to measure more precisely the topology of each of these structures using other methods such as the Minkowsky functionals and/or dimensionless measures such as filamentarity and planarity (e.g. Schmalzing & Buchert 1997; Sahni, Sathyaprakash & Shandarin 1998; Schmalzing et al. 1999). Nevertheless, we leave the topological data analysis for future work.

Next, we show the projected temporal evolution of this same run as viewed from a LOS defined by $\theta_{obs} = 0°$ in Fig. 7. This figure shows how the polarized emission evolves over a period of ~90 Myr. The three snapshots show how the shock discontinuity is travelling from region II towards the right-hand side of our simulation box. Meanwhile, additional shock-induced turbulence develops in the downstream as the discontinuity crosses region III. The first row shows the polarization fraction maps as computed with equation (11). The second and third rows show the Stokes Q and U maps used to compute the corresponding polarization fraction maps, for which we used equations (8–9). We also overplot the Stokes I parameter (i.e. surface brightness) contours in white for completeness. Finally, the fourth row shows the polarization E-vectors as computed with the Stokes Q and U maps and equation (20).

Comparing to the uniform media described in Section 4.1, we find that in the presence of turbulence, the polarization fraction does not increase towards the downstream as in the uniform medium, where we observed a gradient. Instead, a turbulent medium reflects fluctuations in the polarization fraction maps. The shock front is highly polarized, i.e. up to ~70 per cent as the shock sweeps up the transverse components of the magnetic field, effectively aligning the magnetic field vectors. This effect can also be observed in the fourth row of Fig. 7, where the polarization E-vectors at the shock front are mostly aligned with the shock normal. Moreover, downstream of the shock the polarization fraction fluctuates and can decrease to $\lesssim 10$ per cent. In particular, the downstream polarization fraction is affected by magnetic fluctuations in the medium. This is seen in the fourth row of Fig. 7, where the E-vectors are more randomly aligned in the downstream region. Note that at the very end of the downstream region, the polarization fraction is high because this is part of region II with a uniform magnetic field oriented in the x-direction (see Section 2). The E-vectors in this region are perpendicular to the orientation of the magnetic field as shown in Fig. 5. Therefore, this region will be omitted in the subsequent analysis.

In Fig. 8 we show 1D profiles of the surface brightness, polarized intensity, and polarization fraction for the two different turbulent media: $2L/3$, $\mathcal{M} = 3$, and $\theta_{bn} = 0°$ and $L/4$, $\mathcal{M} = 3$, and $\theta_{bn} = 0°$. We show the average over the y-axis for the three quantities and we also show the 1D profile of the polarization fraction selected at a fixed y-position (we selected $y = 0$). The polarized intensity is computed using the following equation:

$$P_\nu = \sqrt{Q_\nu^2 + U_\nu^2}. \tag{23}$$

In both cases, the surface brightness profile is smoother and has higher values than the polarized intensity. This highlights the role of the polarization vectors in the plane of the sky as computed with equations (8) and (9). Due to presence of post-shock turbulence, the profile of the polarization fraction varies considerably in the downstream region. For a fixed y-position, we note that while the shock front reaches a polarization fraction of ~70 per cent, the far downstream region varies from $\lesssim 10$ per cent to 57 per cent in the $2L/3$, $\mathcal{M} = 3$, and $\theta_{bn} = 0°$ case and from $\lesssim 10$ per cent to $\lesssim 50$ per cent in the $L/4$, $\mathcal{M} = 3$, and $\theta_{bn} = 0°$ case. A high polarization fraction of order ~60 per cent at the shock front is found in both models. In the downstream regions, this fraction decreases. This last result is in agreement with what has been recently observed in the Sausage relic (Di Gennaro et al. 2021) where the outermost edge reaches intrinsic polarization values up to ~60 per cent and then the fraction decreases towards the downstream.

The discrepancies between both turbulent media are almost indistinguishable in the polarization profiles, but there are differences that
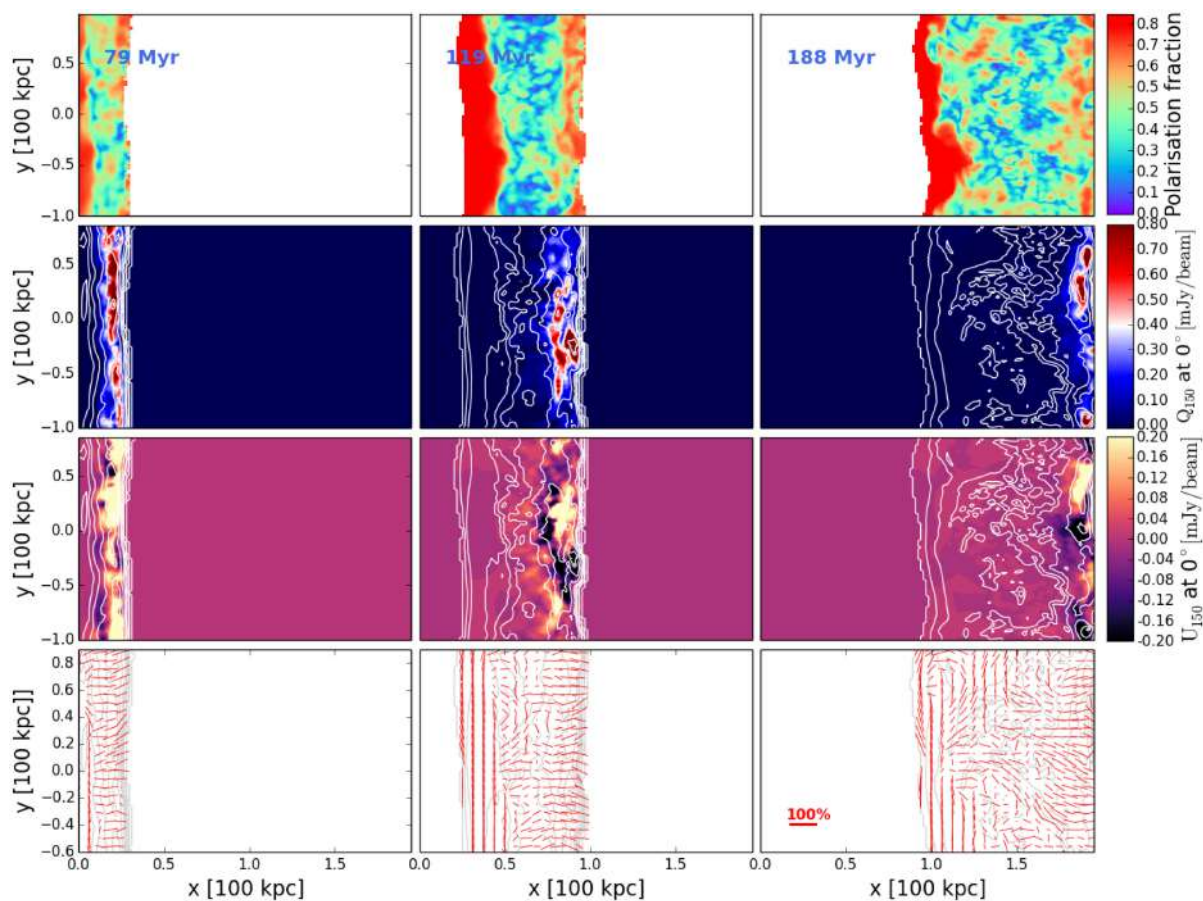
Figure 7. Polarization of the 2*L*/3, $\mathcal{M} = 3$, and $\theta_{\mathrm{bn}} = 0°$ case considering $\theta_{\mathrm{obs}} = 0°$ at 150 MHz. First row: Polarization fraction. Second row: **Stokes Q** parameter maps. Third row: **Stokes U** parameter maps. Fourth row: Polarization *E*-vectors computed with equation (20). We overplot the surface brightness contours in all the maps in the second, third, and fourth rows. We considered a beam of $\theta^2 = 6$ arcsec × 6 arcsec to obtain the units of mJy per beam.

can be better observed in the polarization fraction maps shown in Fig. 9. Again we have excluded the uniform medium in region II. While both turbulent media can have a high polarization fraction at the shock front, the depolarization in the downstream region (considering ∼60 kpc distance from the shock front) is higher for the *L*/4 case than for the 2*L*/3 case. This is expected as smaller magnetic fluctuations will cause more depolarization (see also Fig. 8). This result is linked to the evolution of the magnetic power spectrum. In particular, the characteristic length of the magnetic power spectrum remains smaller in the *L*/4 case compared to that of the 2*L*/3 case during the whole evolution (see λ_{B} in fig. 18 in Paper I). This means that the 2*L*/3 magnetic field stays more coherent at larger scales than the *L*/4 case. Similar polarization profiles have been observed in radio relics, most clearly in the Toothbrush relic (e.g. van Weeren et al. 2012; Rajpurohit et al. 2020b) and in MACSJ0717.5+3745 relic (e.g. Bonafede et al. 2009b; Rajpurohit et al. 2021b). Another example where fractional polarization goes up to 70 per cent is the large relic in the galaxy cluster Abell 2256 (e.g. Owen et al. 2014). However, the relic in Abell 2256 is more complex and cannot be directly compared to our simulations.

In Fig. 9 we also overplotted the polarization *E*-vectors. Both models produce polarization *E*-vectors aligned with the shock normal at the position of the shock front. In order to visualize the overall alignment of the polarization *E*-vectors, we produce probability distribution functions (PDFs) of the polarization *E*-vector angle ψ. In Fig. 10, we show the PDF of these polarization *E*-vectors for

both turbulent media (see corresponding Fig. 9). We also compute the PDF corresponding only to the cells tracking the shock front (see Paper I). This is possible because our numerical implementation relies on tracking the shock discontinuity where the CRe particles are being activated at each time-step. In Fig. 10 we show the normalized PDF of the ∼60 kpc downstream region in purple, and that of the shock front region in green. The PDFs show a similar pattern for both turbulent media. The PDF in the shock front peaks at lower polarization angles, i.e. $|\psi| \leq 30°$. The *L*/4, $\mathcal{M} = 3$, and $\theta_{\mathrm{bn}} = 0°$ case shows a distribution that is narrower than the 2*L*/3, $\mathcal{M} = 3$, and $\theta_{\mathrm{bn}} = 0°$ case. Remembering that $\psi \sim 0°$ is the direction of a polarization *E*-vector parallel to the initial shock normal, Fig. 10 shows that in a turbulent ICM the polarization *E*-vectors tend to align with the shock normal.

Comparing our two turbulent models, we find that the 2*L*/3 turbulence model produces a broader PDF peaking at $\psi \sim 0°$ than the *L*/4 turbulence model. This implies that the final degree of alignment of polarization *E*–vectors at the shock front depends on the distribution of upstream turbulent modes. In particular, these differences stem from the final magnetic power being higher in the 2*L*/3 case than in the *L*/4 case (see magnetic power spectra in figs 16 and 17 in Paper I), and from the larger characteristic scale of the magnetic field in the 2*L*/3 case compared to the *L*/4 case (see λ_{B} in fig. 18 in Paper I). In Paper I, we also found that the standard deviation of the perpendicular component of the magnetic field (with respect to the shock normal), i.e. $B_{\perp} = \sqrt{B_y^2 + B_z^2}$, is modified more
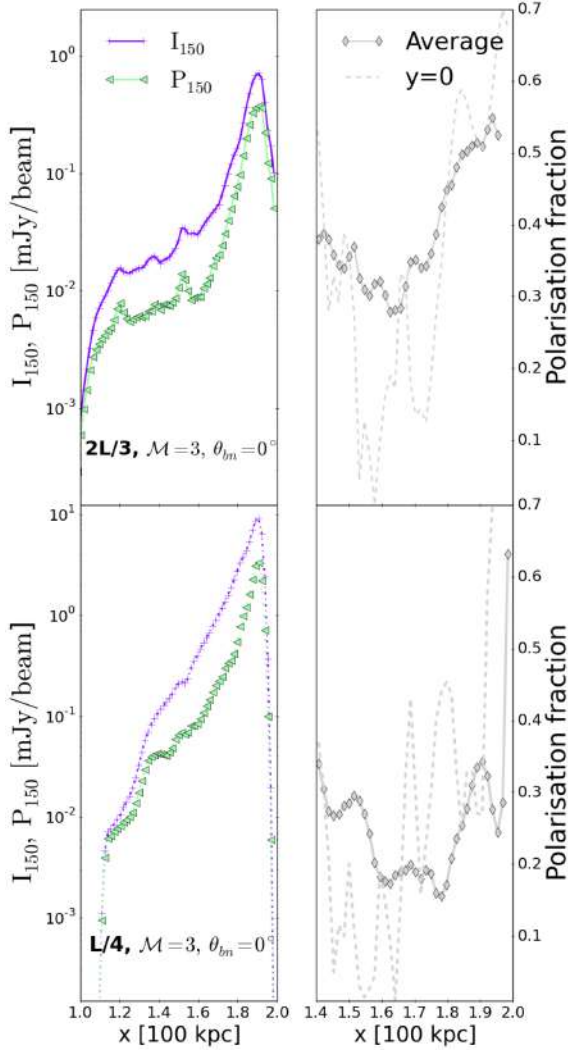
Figure 8. Average 1D surface brightness (*purple crosses*), polarized intensity (*green triangles*), and polarization fraction (*grey diamonds*) profiles considering $\theta_{\mathrm{obs}} = 0°$ at 150 MHz. We also include a 1D polarization fraction profile (*dashed grey line*) corresponding to $y = 0$ in the polarization fraction maps in Fig. 9. The upper panel shows the $2L/3$, $\mathcal{M} = 3$, and $\theta_{\mathrm{bn}} = 0°$ case and the lower panel shows the $L/4$, $\mathcal{M} = 3$, and $\theta_{\mathrm{bn}} = 0°$ case. We considered a beam of $\theta^2 = 6$ arcsec $\times$ 6 arcsec to get the units of mJy per beam, but no smoothing is applied.

than the parallel component due to the shock crossing. Specifically, a shock with strength $\mathcal{M} = 3$ induces a higher increase in the standard deviation of the perpendicular magnetic component of the $2L/3$ case (31 per cent increase) than in the L/4 case (7 per cent).

The orientation or alignment of the polarization *E*-vectors usually gives us an idea on the degree of alignment of the magnetic field. It is therefore also useful to visualize the magnetic field of the Eulerian grid. We show the projected magnetic field weighted by the synchrotron emissivity,

$$B_{\mathrm{proj}} = \frac{\int B \, \mathcal{J}_{\mathrm{syn}} \mathrm{d}z}{\int \mathrm{d}z}, \tag{24}$$

along with the corresponding magnetic field vectors in Fig. 11. The angle of the magnetic field vector was computed by first projecting
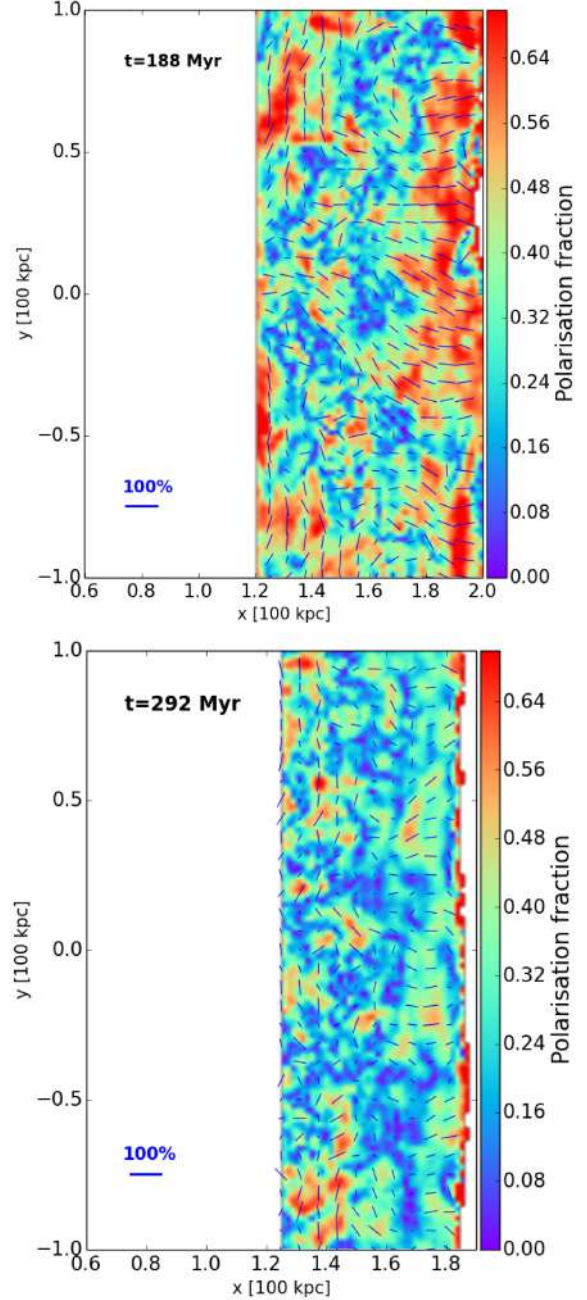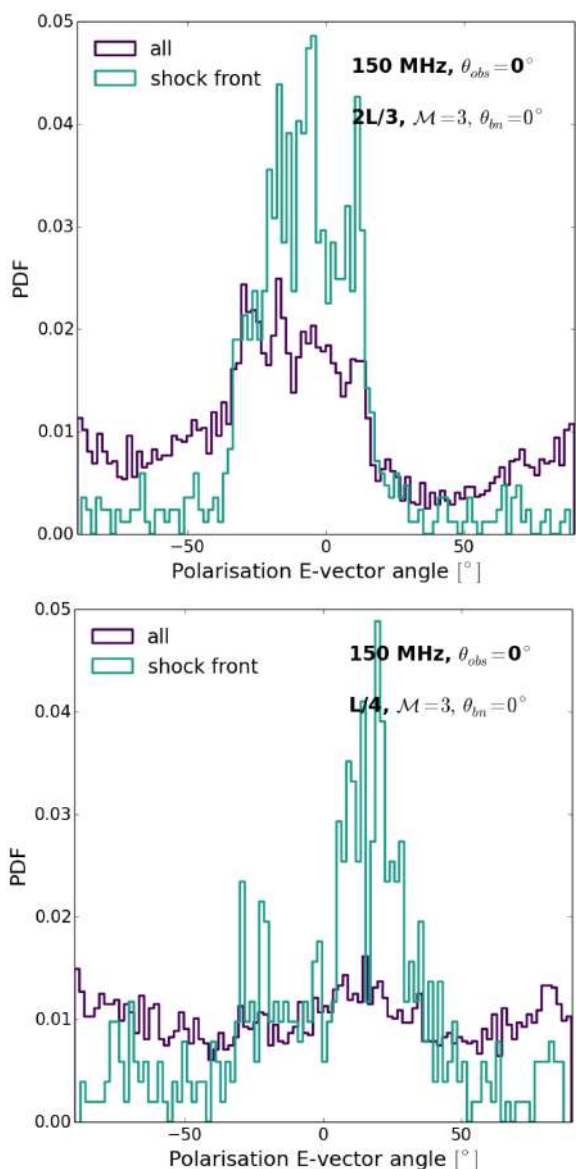

Figure 9. Polarization fraction maps considering $\theta_{\mathrm{obs}} = 0°$ at 150 MHz. The upper panel shows the $2L/3$, $\mathcal{M} = 3$, and $\theta_{\mathrm{bn}} = 0°$ case and the lower panel shows the $L/4$, $\mathcal{M} = 3$, and $\theta_{\mathrm{bn}} = 0°$ case.

the *x*- and *y*-components as in equation (24) and finally computing[4]

$$\psi_B = \arctan\left(\frac{B_y}{B_x}\right). \tag{25}$$

We remind the reader that the projected magnetic field vectors as shown in Fig. 11 may not be identical to the polarization *B*-vectors. In order to understand the orientation of the polarization *B*- and *E*-vectors, we show a sketch in Fig. 12 explaining how the individual magnetic field components along one particular LOS contribute to the final orientation. There are two possibilities leading to polarization:

[4]Here also $\arctan(\theta)$ considers the four quadrants, i.e. $\theta \in [-\pi, \pi]$

Figure 10. PDF of the polarization *E*-vector angles as obtained from the maps considering $\theta_{\mathrm{obs}} = 0°$ at 150 MHz. The purple PDF corresponds to a ~ 60 kpc downstream region (see Fig. 9) and the green PDF is restricted to the shock front region. The upper panel shows the 2*L*/3, $\mathcal{M} = 3$, and $\theta_{\mathrm{bn}} = 0°$ case and the lower panel shows the *L*/4, $\mathcal{M} = 3$, and $\theta_{\mathrm{bn}} = 0°$ case.

(i) *A uniform homogeneous magnetic field*: Here all the magnetic field components along the LOS would contribute to the same direction.

(ii) *The compression of a tangled magnetic field*: Here an anisotropic distribution of the magnetic field components (in the B_x–B_y plane in our case) leads to a specific alignment of the polarization vectors (see also Burn 1966). Without compression, a randomly oriented magnetic field that produces a perfectly isotropic distribution in the B_x–B_y plane will not produce polarization.

The first possibility was already shown in Section 4.1, while the second possibility explains the results shown in this section. In Fig. 13 we show the distributions in the B_x–B_y plane for our two turbulent models by considering two particular LOS. Each LOS was selected to be at the location of the shock front (see box coordinates in Fig. 13). The distributions are in general not isotropic due to the compression
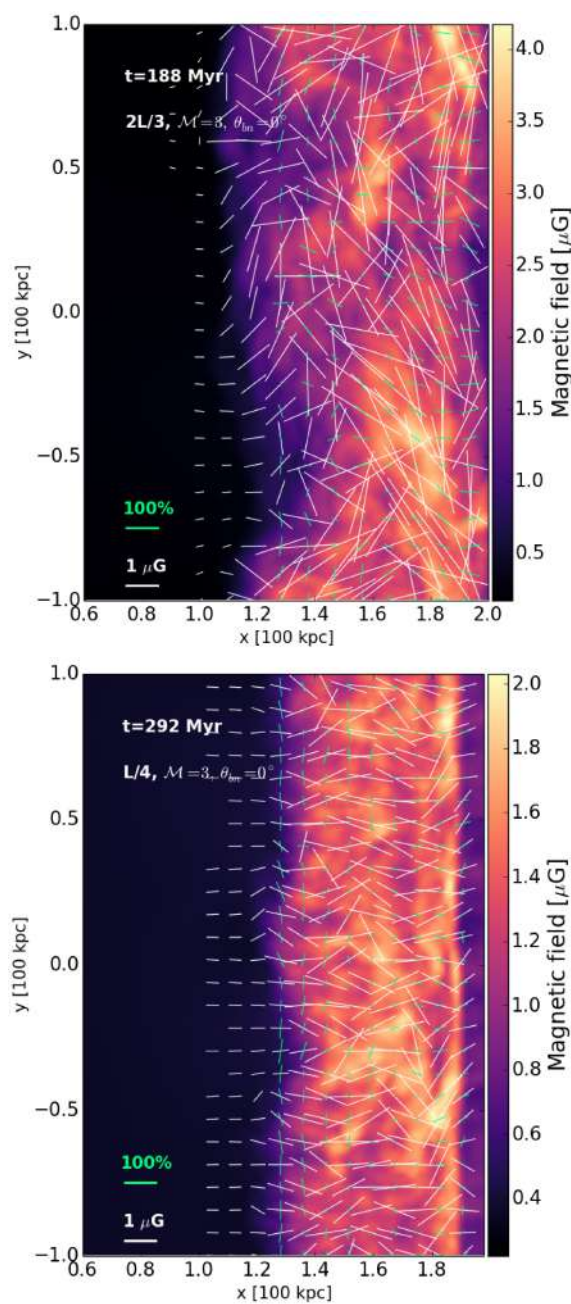
Figure 11. Projected magnetic field of the Eulerian grid. The magnetic field vectors are shown in white and the polarization *E*-vector in green. The upper panel shows the 2*L*/3, $\mathcal{M} = 3$, and $\theta_{\mathrm{bn}} = 0°$ case and the lower panel shows the *L*/4, $\mathcal{M} = 3$, and $\theta_{\mathrm{bn}} = 0°$ case.

of the shock. The B_x–B_y distribution can be seen as bivariate data with a covariance matrix describing an ellipse. The eccentricity of the covariance ellipse is related to the anisotropy of the distribution. We therefore characterize each B_x–B_y distribution by computing a 3σ covariance confidence ellipse (see contours in Figs 13 and 14). The more anisotropic the distribution is, the more elongated the covariance ellipse will be. The alignment of the ellipse major axis then defines the alignment of the polarization *B*-vector and as a result, the minor axis defines the alignment of the polarization *E*-vector. Due to beam smearing, we would always have contamination coming from various LOS in observations. It is therefore useful to visualize
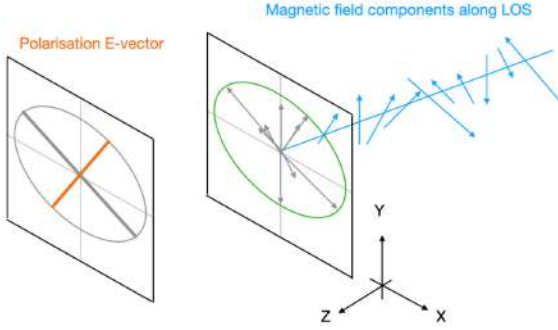
Figure 12. Schematic of different magnetic field components that contribute to one LOS as seen from the *z*-axis. If the final distribution of the magnetic field components is anisotropic with a preferred direction, then we would observe an ellipse in the B_x–B_y plane. The alignment of the polarization *B*-vector (*E*-vector) is defined then by the direction of the major (minor) radius of the ellipse.

the B_x–B_y distribution for a region instead of a single LOS. In Fig. 14 we show the corresponding distributions for a fixed *x*-coordinate and consider all the contributions from all the *y*-coordinates. In this case, we show the B_x–B_y distribution for regions in the upstream (~ 30 kpc ahead of the shock front), at the shock front and in the downstream (~ 20 kpc behind of the shock front) for our two turbulent models at a different simulation time[5] (see text in each panel of Fig. 14). Both turbulent models show similar trends, the B_x–B_y distribution is more anisotropic at the shock front and then it becomes more isotropic further in the downstream, i.e. the emission is less polarized in the downstream. The anisotropy at the shock front is observed as a more elongated ellipse in the B_y component due to the fact that the shock compression affects only the components that are perpendicular to the shock normal (i.e. B_y and B_z in our set-up). This explains the overall alignment of the polarization *E*-vectors in the direction of the shock normal (i.e. *x*-direction in our set-up) at the shock front. Each LOS in Fig. 14 is coloured according to the polarization fraction value at every (x, y) position in the corresponding polarization fraction map. One can observe that the highest polarization fraction is indeed observed at the shock front. This confirms our obtained trends in the polarization fraction maps as well as the alignment of the polarization *E*-vectors (see Figs 9 and 11).

Having characterized the B_x–B_y distribution with the covariance ellipse, we can further investigate the expected decrease of anisotropy towards the downstream for each turbulent model compared to the upstream distribution. In Fig. 15 we show the characteristics of the covariance ellipses as shown in Fig. 14. The ellipse centre corresponds to the mean of the distribution, whereas the extent of the ellipse axes defines the anisotropy of the distribution. The way the distribution becomes more isotropic towards the downstream can be mainly seen in the lower panel of Fig. 15 where the size of both axes start to have more similar sizes towards the downstream. In other words, the major axis of the ellipse will start to decrease towards the downstream up to the point where its size is comparable with the minor axis. The 2*L*/3 model shows more magnetic amplification than the *L*/4 model as can be observed in the upper panel of Fig. 14 and

---

[5]Note that the simulation times selected for Fig. 13 correspond to the same simulation times discussed previously in this section where the shock front has reached the right computational boundary, whereas the simulation times selected for Fig. 14 correspond to an earlier phase of the shock propagation that allow us to study the upstream B_x–B_y distribution.
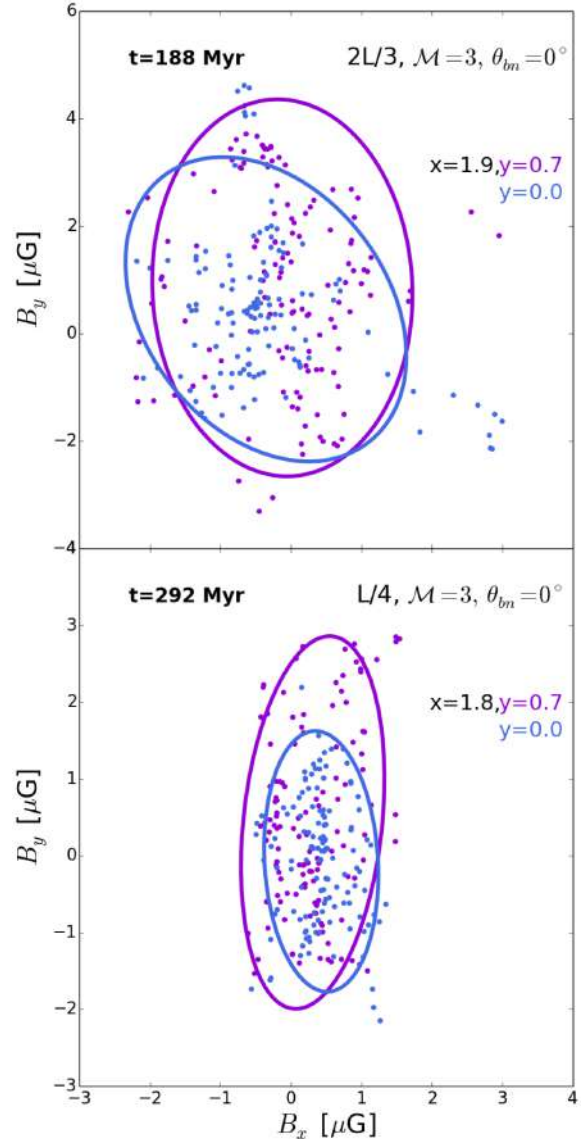
Figure 13. B_y–B_x distribution of magnetic field components along two LOS. The LOS are taken at a fixed box coordinates *x* and *y* (see e.g. Fig. 9). *Upper panel*: 2*L*/3, $\mathcal{M} = 3$, and $\theta_{bn} = 0°$ case. *Lower panel*: *L*/4, $\mathcal{M} = 3$, and $\theta_{bn} = 0°$ case. The *x* coordinate is located at the position of the shock front and we show two different LOS by selecting two *y* positions (purple and blue). A 3σ covariance confidence ellipse is shown in each plot.

in agreement with fig. 8 of Paper I. On the other hand, due to this higher magnetic amplification, the B_x–B_y distribution will become isotropic at a shorter distance from the shock front in the 2*L*/3 case than in the *L*/4 case (see lower panel in Fig. 15). This clearly shows that the degree of depolarization downstream of the shock depends on the properties of the underlying turbulent medium. Hence, it can inform us also on the properties of the ICM upstream of the shock.

In summary, the shock compression of a turbulent ICM leads to specific characteristics in polarization: (1) a high polarization fraction at the shock front and a decrease towards the downstream region; and (2) an alignment of the polarization *E*-vector with the shock normal. The depolarization in the downstream region is subject to the properties of the underlying pre-shock turbulent medium. In particular, it is subject to how the B_x–B_y distribution becomes more isotropic towards the downstream region. We find that the 2*L*/3 case
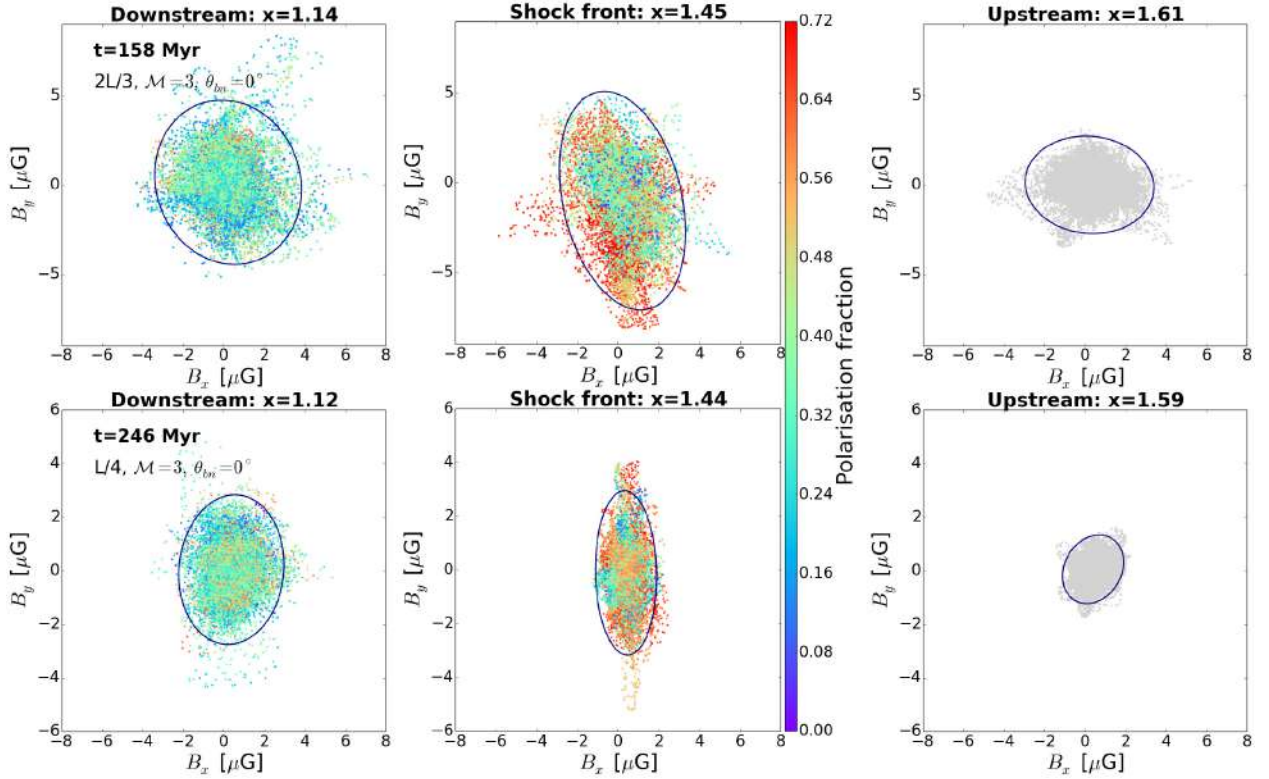
Figure 14. B_x–B_y distribution of magnetic field components along various LOS (similar to Fig. 13). In this case, we fix only the x position and we present all the different LOS along the y-axis. The first, second, and third columns correspond to a specific x position at the downstream, shock front, and upstream, correspondingly. *Upper row*: $2L/3$, $\mathcal{M} = 3$, and $\theta_{bn} = 0°$ case. *Lower row*: $L/4$, $\mathcal{M} = 3$, and $\theta_{bn} = 0°$ case. The scatter plots presented in the first two columns are coloured according to the value of the polarization fraction in the polarization fraction maps at every (x, y) position (see Fig. 9). Since the upstream is not polarized, we present the distribution without colouring. A 3σ covariance confidence ellipse is shown in each of the distributions.
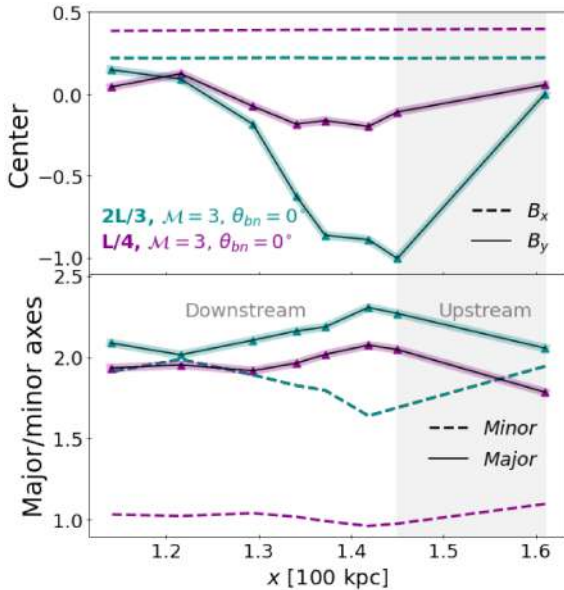

Figure 15. Centre and minor and major axes of the covariance confidence ellipse fitted to the B_x–B_y distributions as seen in Fig. 14 in the upstream, shock front, and downstream regions. *Upper panel*: Mean given by the ellipse centre. The dashed (solid) lines correspond to the mean values of the B_x (B_y) component. *Lower panel*: Minor (dashed lines) and major (solid lines) axes of the fitted ellipse. The values are given in units of μG.

tends to isotropize the B_x–B_y distribution at a distance closer to the shock front than the L/4 case.

4.3 The effect of internal Faraday rotation

There are two contributions to consider when the polarized signal propagates through a magnetized medium along the LOS: internal RM (intrinsic to the source) and external RM (external to the source). The external contributions to the observed RM can come from the foreground intergalactic medium, e.g. the contribution from the Milky Way, and from the foreground ICM in the case that the relic is located behind the cluster. The local Galactic foreground from the Milky Way can in general be calibrated with RM grid data from our Galaxy (e.g. Hutschenreuter & Enßlin 2020). On the other hand, the contribution of a larger foreground ICM to the external Faraday rotation is subject to the location of the relic within the galaxy cluster. Observationally, the external contribution can be constrained using RM synthesis and QU-fitting techniques (e.g. Anderson et al. 2018; Stuardi et al. 2019; Lerato Sebokolodi et al. 2020; Purcell et al. 2020). Theoretically, it can also be studied with cosmological simulations (e.g. Vazza et al. 2018; Wittor et al. 2019). Our simulations are dedicated to study a small region of the ICM, 400 kpc × 200 kpc × 200 kpc (see Section 2), and therefore can only yield the internal contribution. In this section, we focus on the Faraday rotation contributed by the ICM within our computational box (e.g. internal RM).

In Fig. 16 we show the PDF of the RM for both turbulent media: at $t = 188$ Myr for the $2L/3$ case (upper panel) and at $t =$
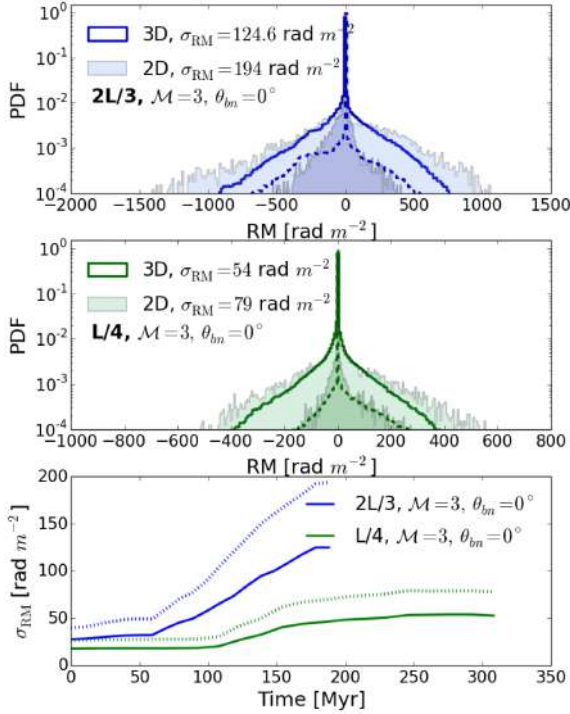
Figure 16. PDF of the RM for both turbulent media integrated along the z-axis: at $t = 188$ Myr for the 2*L*/3 case (*upper panel*) and at $t = 292$ Myr for the *L*/4 case (*middle panel*). The step PDF corresponds to the 3D distribution and the step-filled PDF corresponds to the 2D distribution as integrated over the whole box (200 kpc) along z. The dashed lines correspond to the 3D weighted distribution and the PDFs with higher less transparency correspond to the 2D weighted distribution (see equations 26–27). *Lower panel*: Evolution of the standard deviation σ_{RM} of the 3D (solid lines) and 2D (dotted lines) distribution for both media.

292 Myr for the *L*/4 case (middle panel). We show the PDF for the 3D distribution of RM (measured within single cells) and the 2D distribution obtained after integrating along the full LOS in the z-direction. We note how the RM strongly depends on the density and magnetic field fluctuations in each of our turbulent media, and also how the distribution of the RM evolves in time as the shock is propagating through the ICM. In general, the compression of the turbulent magnetic field increases the RM over time. For the 2*L*/3 turbulence model, we obtain RM values ranging from ± 200 rad m^{-2} at the early stages of the shock propagation, up to ± 1000 rad m^{-2} at the late stages of the shock propagation (see 3D distribution in the upper panel of Fig. 16). In this case, we can also see that the RM distribution at the late stages is non-Gaussian. This non-Gaussianity has also been observed in cosmological simulations (see e.g. Wittor et al. 2019). For the L/4 turbulence model, we obtain RM values ranging from ± 100 rad m^{-2} at the early stages of the shock propagation to ± 400 rad m^{-2} at the late stages of the shock propagation (see 3D distribution in the middle panel of Fig. 16). At the snapshot shown in the upper and middle panels of Fig. 16, the 2*L*/3 case has a mean RM value of ~ -6 rad m^{-2} and a standard deviation of the RM of about $\sigma_{RM} = 194$ rad m^{-2}, whereas the L/4 case has a mean RM value of ~ 1 rad m^{-2} and a standard deviation of the RM of about $\sigma_{RM} = 80$ rad m^{-2}. In observations, the RM can only be inferred for regions that show radio emission. Therefore, we also compute the PDF of the RM weighted by the radio emission

regions,

$$RM = 0.812 \text{ rad m}^{-2} \sum_{i=0}^{n} n_e B_{\parallel} w_i \, dl, \tag{26}$$

where $n = n_z$ (total number of cells in the z-axis) for the 2D distribution and $n \in [1, n_z]$ for the 3D distribution. The weight function w_i is defined as

$$w_i = \begin{cases} 1 & \text{if } \Lambda \neq 0, \\ 0 & \Lambda = 0, \end{cases} \tag{27}$$

where $\Lambda = \mathcal{J}_\nu$ (emissivity). We selected the emission at 150 MHz as a weight for Fig. 16.

The PDF of the RM (both in 2D and 3D) narrows when taking into account only the radio emitting cells. For the 2*L*/3 turbulence, we obtain RM values of ± 500 rad m^{-2} in the 3D distribution at $t = 188$ Myr (see the dashed blue line PDF in Fig. 16). For the L/4 turbulence, we obtain RM values of ± 200 rad m^{-2} in the 3D distribution at $t = 292$ Myr (see the dashed green line PDF in Fig. 16). Note that we have arbitrarily selected a weighting such that the RM reflects radio regions with emissivities larger than the zero. None the less, it is straightforward to see that the PDF could narrow even more if we were to select e.g. the brightest radio cells. Keeping this in mind, these values are in the ballpark of typically observed RM at the outskirts of clusters (e.g. Böhringer, Chon & Kronberg 2016 for a catalogue of RM of extragalactic polarized sources) or for individual sources (see e.g. Johnston-Hollitt & Ekers 2004; Bonafede et al. 2013; Rajpurohit et al. 2020b; Di Gennaro et al. 2021).

In Paper I we showed that the amplification of the magnetic field proceeds in a different manner for the 2*L*/3 and *L*/4 cases. In the same way, we show how the standard deviation of the RM, σ_{RM} changes in time for both models in the lower panel of Fig. 16. As can be seen, the RM changes can differ considerably depending on the initial ICM conditions. The σ_{RM} will increase as the shock continues to propagate through each medium. In particular, the σ_{RM} increases more for the 2*L*/3 case than for the L/4 case. This is line with the increment of the standard deviation of the magnetic field (see fig. 7 in Paper I). Since the rate of change will depend on the initial magnetic field strength, the rms Mach number in the medium, energy ratios, the characteristic scale of the underlying fluctuations, and the strength of the shock, it is not possible yet to fully parametrize its evolution as a function of environmental parameters.

Next we compute the RM contribution to the polarization in post-processing. The polarization emissivity can be written as

$$\mathcal{P}_\nu = \mathcal{J}_{pol}(\nu_{obs}, x, y, z) \exp\left[2i(\hat{\chi} + RM\lambda_{obs}^2)\right], \tag{28}$$

where we have used equation (18). It is then easy to see that the real part of equation (28) gives the Stokes Q parameter and the imaginary part gives the Stokes U parameter, equivalent to equations (8–9). After some algebra we can finally obtain the Stokes Q and U maps with the RM contribution as

$$Q_\nu = \int \mathcal{J}_{pol}[\cos(2\hat{\chi})\cos(2RM\lambda_{obs}^2) \\ - \sin(2\hat{\chi})\sin(2RM\lambda_{obs}^2)]dz, \tag{29}$$

$$U_\nu = \int \mathcal{J}_{pol}[\sin(2\hat{\chi})\cos(2RM\lambda_{obs}^2) \\ + \cos(2\hat{\chi})\sin(2RM\lambda_{obs}^2)]dz. \tag{30}$$

The polarization fraction with the RM contribution is finally computed in the same way as in equation (11).
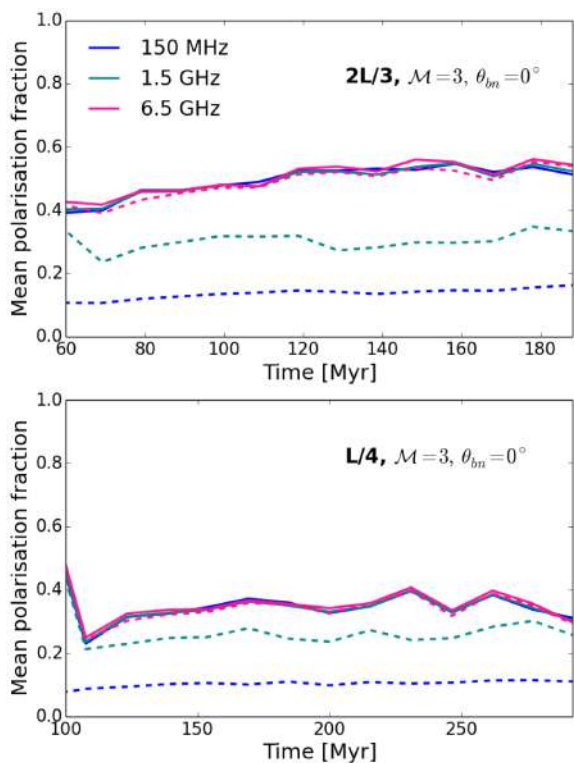
Figure 17. Evolution of mean polarization fraction at the shock front for the 2*L*/3, $\mathcal{M} = 3$, and $\theta_{bn} = 0°$ case (*upper panel*) and the *L*/4, $\mathcal{M} = 3$, and $\theta_{bn} = 0°$ case (*lower panel*). The *solid lines* correspond to the polarization fraction without RM contribution and the *dashed lines* correspond to the polarization fraction with RM contribution. Note that we show the time evolution since the shock front enters the turbulent region III.

We start by showing how the polarization fraction evolves at the location of the shock front at different frequencies. In Fig. 17 we show the mean polarization fraction as function of time for both turbulent media. The mean was computed by taking only into account the polarization fraction at the shocked cells (similar to Section 4.1). We also show how the mean polarization fraction decreases when the Faraday rotation is taken into account for different frequencies (see dashed lines in Fig. 17). We find that at 150 MHz the RM contribution depolarizes both media down to ∼10–20 per cent. Indeed, observed radio relics are not expected to show significant polarization at such low frequencies (Brentjens 2008; Pizzo et al. 2011; Ozawa et al. 2015). At higher frequencies, the Faraday rotation effect becomes less significant. The RM contribution at 6.5 GHz is negligible leading to minor or almost no changes in the evolution of the mean polarization fraction. On the other hand, the RM contribution at 1.5 GHz depolarizes more the 2*L*/3 medium than the *L*/4 medium due to the larger RM values in the former case (see Fig. 16).

The effect of Faraday depolarization at 150 MHz can be better visualized in Fig. 18 where we show the polarization E-vectors with the RM contribution for both turbulent media. We also show the corresponding polarization E-vectors without RM as previously shown in Fig. 9. The RM introduces extra rotation in the polarization E-vectors and it depolarizes the downstream and shock front regions, as expected. As shown in Fig. 17, the mean polarization fraction at the shock front reaches ∼10 per cent for the L/4 case, while it reaches ∼20 per cent for the 2L/3 case. Note that these values are derived from the $\theta_{obs} = 0°$, i.e. edge-on view of the shock. For other viewing angles where $\theta_{obs} \lesssim 90°$, we expect a lower, yet not
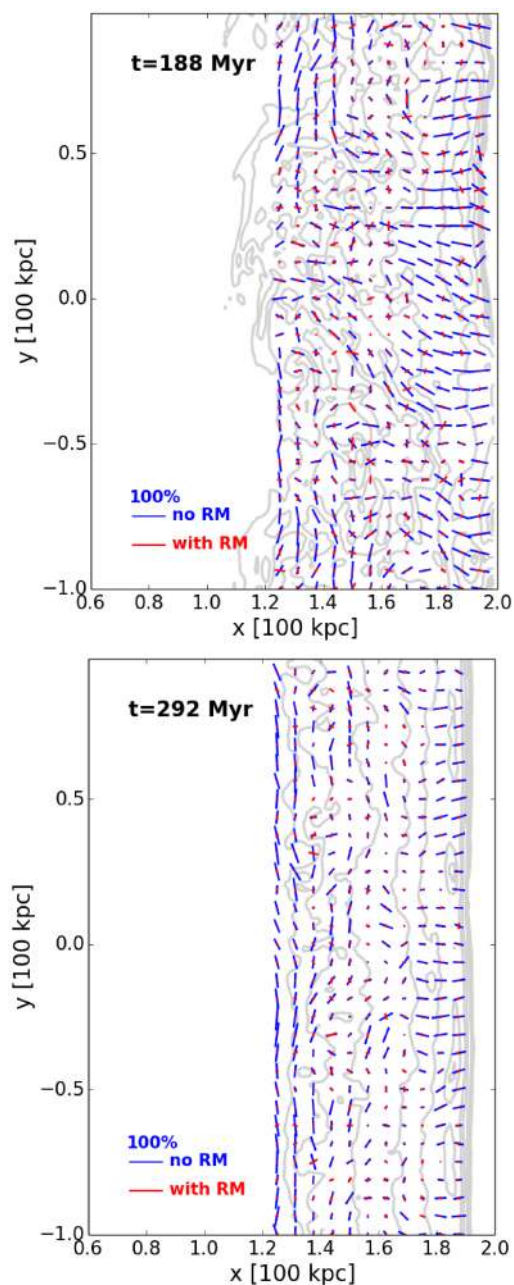
Figure 18. Polarization E-vectors with (red) and without (blue) the RM contribution considering $\theta_{obs} = 0°$ at 150 MHz showing the effect of intrinsic RM depolarization. The upper panel shows the 2*L*/3, $\mathcal{M} = 3$, and $\theta_{bn} = 0°$ case and the lower panel shows the *L*/4, $\mathcal{M} = 3$, and $\theta_{bn} = 0°$ case. The grey contours show the surface brightness.

null, polarization fraction. The multiscale structure of a turbulent magnetic field can allow some components to contribute to the linearly polarized emission along the LOS (see Section 3). Since it is non-trivial to pin-point the relation between expected polarization trends and the contributing magnetic components along different LOS, we leave a complete study on viewing angles for future work.

We computed the PDF of the polarization E-vectors for both turbulent media, with and without the RM contribution. We show the PDFs in Fig. 19 for the three different frequencies considered in this work. We additionally show the PDF corresponding only to the cells tracking the shock front (same as in Fig. 10). It becomes then
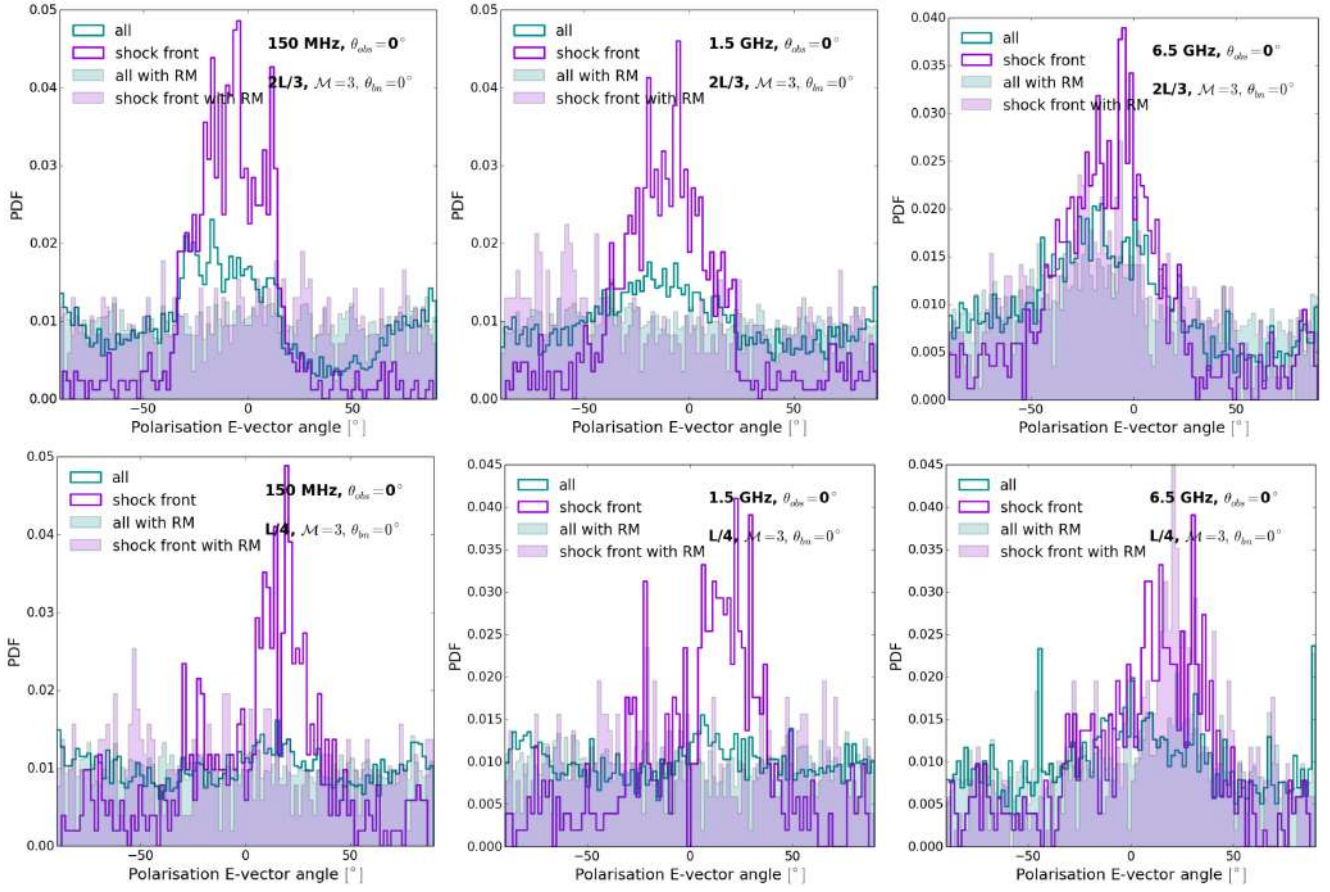
Figure 19. PDFs of the polarization *E*-vector angle with (step) and without (step-filled) the RM contribution. We show $\theta_{\rm obs} = 0°$ at different frequencies. The first row shows the 2*L*/3, $\mathcal{M} = 3$, and $\theta_{\rm bn} = 0°$ case, and the second row shows the *L*/4, $\mathcal{M} = 3$, and $\theta_{\rm bn} = 0°$ case. The first, second, and third columns correspond to the frequencies 150 MHz, 1.5 GHz, and 6.5 GHz. We show the PDF of $\sim$60 kpc in the downstream region in darkcyan and that of the shock front in darkorchid.

more evident that the alignment or orientation of the polarization E-vectors with the shock normal will persist at 6.5 GHz, regardless of the properties of the turbulent medium. On the other hand, already at 1.5 GHz, the RM contribution can be relevant depending on the type of underlying turbulence. These differences are again due to the magnetic power and to the standard deviation of the magnetic field as discussed in Section 4.2. In Paper I, we showed that a $\mathcal{M} = 3$ shock induces a larger increase in the standard deviation of the magnetic field in the 2L/3 case, compared to the L/4 case. This can be also seen in the lower panel of Fig. 16 where we show the evolution of the RM standard deviation of both cases.

From the results in this section we can already confirm that in the presence of turbulence, the impact of internal RM on the observable polarized emission is significant at LOFAR-alike or lower frequencies. Its contribution will effectively depolarize the source, likely explaining the typically reported lack of (or little) polarized emission in low-frequency observations of radio relics. Conversely, our study shows that the alignment of the polarization *E*-vectors with the shock normal and a high polarization fraction at the shock front are results that should persist with or without the contribution of internal RM at about 6.5 GHz, or larger. Finally, we find that these results are more dependent on the turbulent conditions when observed at 1.5 GHz. We expect that the exact relation between the observed changes in the polarization properties and turbulence parameters might be constrained with future simulations that consider a large scan of model parameters prescribing the level of turbulence in the ICM.

As a side note, we note that further depolarization can occur due to instrumental effects such as bandwidth depolarization. The polarization angle rotates over the bandwidth effectively depolarizing the signal (see Klein & Fletcher 2015). In order to minimize this effect, the observing bandwidth is subdivided into many sub-bands or channels and the RM synthesis technique is applied (Brentjens & de Bruyn 2005). In the case of LOFAR, a typical observing sub-band is 0.2 MHz and there are 4–16 channels in the sub-band (van Haarlem et al. 2013). Assuming a typical observation with four channels, the channel width is $\sim$0.05 MHz. At 1.5 GHz the typical channels widths are $\sim$1 MHz and at 6.5 GHz $\sim$10 MHz. The bandwidth depolarization is given by (see chapter 3 of Klein & Fletcher 2015)

$$\pi_{\nu,b.d} = \pi_\nu \frac{\sin \Delta \Psi}{\Delta \Psi}, \tag{31}$$

where b.d stands for bandwidth depolarization, Π_ν is the polarization fraction defined in equation (11), and

$$\Delta \Psi = -2\lambda_0^2 RM \frac{\Delta \nu}{\nu_0}, \tag{32}$$

where λ_0 and ν_0 are the observing central wavelength and frequency, respectively. In Table 2 we show the amount of bandwidth depolarization expected at 150 MHz, 1.5 GHz, and 6.5 GHz for the two turbulent models. Note that here we compute $\Delta \Psi$ assuming the maximum RM to be conservative (see Fig. 16). This will make a small difference at 150 MHz in the polarization fraction only in the 2L/3 model.

Table 2. First column: Central frequency studied in this work. Second column: Typical channel width from observations at the selected frequencies. Third column: Bandwidth depolarization term in equation (31) using the maximum RM value showed in the weighted PDF in Fig. 16 for the 2L/3 case ($\sim$500 rad m^{-2}). Fourth column: Same as third column but for the L/4 case ($\sim$200 rad m^{-2}).

ν_0 [GHz]	$\Delta\nu$ [MHz]	$\frac{\sin\Delta\Psi}{\Delta\Psi}\big|_{2L/3}$	$\frac{\sin\Delta\Psi}{\Delta\Psi}\big|_{L/4}$
0.15	0.05	0.73	0.95
1.5	1.0	0.99	1.0
6.5	10	1.0	1.0

Table 3. Restoring beam sizes typical of the *Very Large Array* (*VLA*; in either configuration BCD or ABCD) assumed for smoothing the emission maps. We considered a redshift of $z = 0.22$ to quote the corresponding linear length of the full width half-maximum (FWHM).

Beam	FWHM [kpc]
2 arcsec $\times$ 2 arcsec	7.4
5 arcsec $\times$ 5 arcsec	18.4
12.5 arcsec $\times$ 12.5 arcsec	46.1

Nevertheless, if we take the mean RM to be the representative value in equation (32), the polarization fraction will not change. Since the maximum RM values are only achieved at certain cells, it is overall safe to say that the effect of bandwidth depolarization can be ignored in this work.

As a final note, turbulence may extend to smaller scales than our current resolution. Hence, in reality, we would find at each cell a distribution of magnetic field vectors that may lead to extra depolarization at each cell. In order to asses this possible outcome, we can assume as a first-order approximation that the slope for the magnetic power spectrum is the same as the Kolmogorov $k^{-5/3}$ spectrum. In this case, let us assume that in a cell the magnetic field fluctuates on scales that are a fraction of our resolution, i.e. $f\Delta x$ with $0 \le f \le 1$. For $f = 0.1$, we would obtain a fluctuations of about $\sim 0.1^{5/3} \sim 0.02$, and for $f = 0.3$ of about $\sim 0.3^{5/3} \sim 0.13$. Sokoloff et al. (1998) estimated the depolarization fraction due to an isotropic random magnetic field superimposed on a regular magnetic field. We considered their equation (24),

$$\pi_{\nu,S} = \pi_\nu \frac{\overline{B}_\perp^2}{\overline{B}_\perp^2 + 2\sigma_B^2} = \pi_\nu \, W_S, \qquad (33)$$

where $\Pi_{\nu,S}$ denotes the polarization fraction in Sokoloff's work, σ_B is the 1D standard deviation of the random magnetic field, and $\overline{B}_\perp$ is the mean magnetic field perpendicular to the LOS. The W_S value from the turbulent random magnetic field is estimated to be ~ 0.92–0.99 considering $f = 0.1$ and $f = 0.3$.[6] Therefore, the intrinsic polarization could be lower by a ~ 0.92–0.99 due to the tangled field on unresolved scales. It shall be noted that compression of a merger shock may also cause the unresolved magnetic field distribution to be anisotropic, hence the depolarization could be lower than estimated above. In future work, we will asses this by analysing higher resolution simulations.
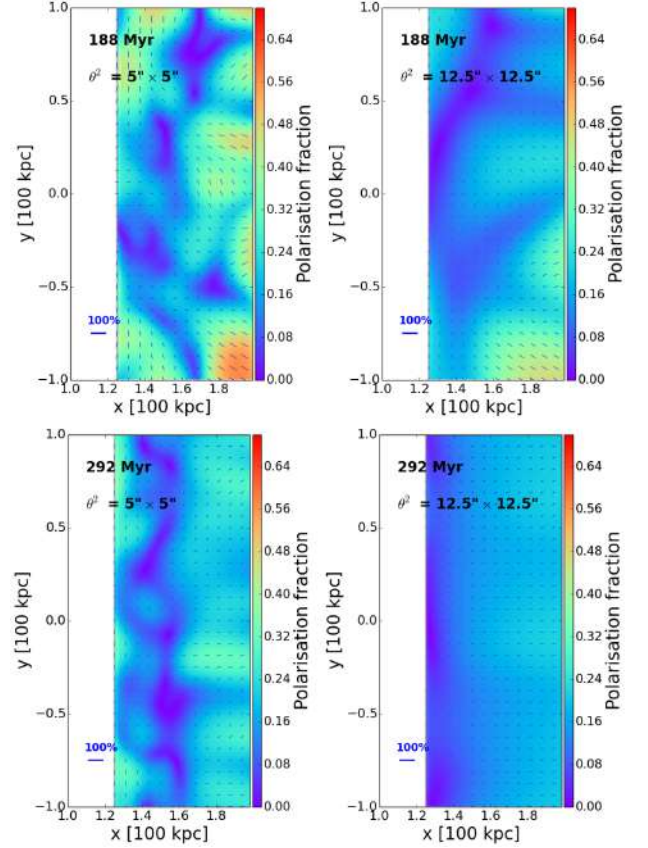
4.4 Beam effects and depolarization

The observed polarized emission is inevitably tied to a beam size. The selected beam size can change the observed polarization fraction, as well as the observed orientation of the polarization E- and B-vectors. This effect is known as beam depolarization, and could be stronger when the scale of magnetic fluctuations is smaller than the beam size. In this section we study how different beam sizes change the results from Section 4.3. We consider different beam sizes in order to smooth the I_ν, Q_ν, and U_ν maps. We assume a redshift $z = 0.22$ corresponding to that of the merging galaxy cluster 1RXS J0603.3+4214 that hosts the Toothbrush relic. We show the beam characteristics in Table 3.

---

[6]Note that the 3D components are related to the 1D component through $\sigma_x^2 + \sigma_y^2 + \sigma_y^2 = 3\sigma_B^2$

Figure 20. Polarization fraction maps smoothed considering $\theta_{\rm obs} = 0°$ at 6.5 GHz. The first row shows the 2L/3, $\mathcal{M} = 3$, and $\theta_{\rm bn} = 0°$ case and the second row shows the L/4, $\mathcal{M} = 3$, and $\theta_{\rm bn} = 0°$ case. The first and second columns correspond to beam sizes of 5 arcsec $\times$ 5 arcsec and 12.5 arcsec $\times$ 12.5 arcsec, respectively. We overplot the polarization E-vectors obtained with the smoothed Q and U maps and equation (20). Note that here we have included the internal RM contribution.

In Section 4.3 we showed how internal Faraday rotation depolarizes the emission mainly at 150 MHz. Therefore, we focus on discussing beam depolarization at 1.5 and 6.5 GHz in this section.

In Fig. 20 we show the polarization fraction maps at 6.5 GHz smoothed on the scales of two different beams: 5 arcsec $\times$ 5 arcsec and 12.5 arcsec $\times$ 12.5 arcsec. These maps were obtained by first applying Gaussian smoothing with a kernel corresponding to the desired FWHM in the I_ν, Q_ν, and U_ν maps. In this case, we have used equations (29–30) where the Faraday rotation effect is taken into account in order to show a more realistic scenario. In the first row, we show the 2L/3, $\mathcal{M} = 3$, and $\theta_{\rm bn} = 0°$ case and the second

row, the $L/4$, $\mathcal{M} = 3$, and $\theta_{bn} = 0°$ case. The lower the resolution, the lower the polarization fraction, i.e. we observe beam depolarization when going to larger beams/lower resolutions.

The decreasing amplitude of fluctuations in the polarization fraction is also evident at lower resolutions for both turbulent length scales. For example, at the lowest resolution, i.e. the beam of 12.5 arcsec × 12.5 arcsec, the local polarization fraction reaches up to ∼45 per cent and ∼20 per cent at the shock front in the $2L/3$ and $L/4$ cases, respectively.

Having a higher polarization fraction at regions of the shock front and depolarization in the downstream even at lower resolution seems to be a pattern that cannot be reproduced with a uniform medium. We saw in Section 4.1 that a uniform medium produces a gradient with the highest values at the downstream region and the lowest at the shock front (see Fig. 5). This gradient in the uniform runs remains observable when considering the three different beam sizes. We show this result in Fig. A1 of Appendix A. Therefore, Fig. 20 shows that even at low resolution, we would distinguish between a turbulent or uniform media at the relic position. We also can confirm that a turbulent medium with smaller magnetic fluctuations is more affected by beam depolarization. Overall, Fig. 20 shows drastic morphological changes in the observed polarized emission due to a limited resolution.

The PDF of the polarization E-vector angles at 1.5 and 6.5 GHz can be observed in Fig. 21. At higher frequencies, the $2L/3$ case shows a stronger alignment of the polarization E-vectors with the x-axis (which roughly corresponds to the direction of the shock's normal vector). This can be seen in the shape of the PDF with no smoothing, whereas the PDF of the $L/4$ case is in general flatter than the PDF for the $2L/3$ case, confirming the more random orientation of polarization vectors. Note that here we are considering the emission from the entire downstream region and not just the shock front as in Fig. 10. An angular resolution of 2 arcsec leaves the shape of the PDF roughly unchanged in all runs (see Fig. 19). However, poorer resolutions change significantly the orientation of the polarization E–vectors. In particular, a 12.5 arcsec resolution tend to result in smaller angles of the E–vectors (defined with respect of our x-axis), i.e narrowing the PDF. The reason is that larger beams give more weight to the brightest regions where the E-vector is largely aligned with the shock normal, i.e $\psi \sim 0°$ as shown in Fig. 10 (see also Figs 7 and 8).

This effect is evident at 6.5 GHz, and it becomes more subtle at 1.5 GHz. As discussed in Section 4.3, the RM contribution at 1.5 GHz can be significant and it depends on the turbulent medium. Depolarization could lead to a flatter PDF of the polarization E-vector angle, with no particular preference or peak at a certain angle. But even in this case, a lower resolution image will tend to pick up the brightest regions and to narrow the range of the observed PDF. Therefore, a lower resolution image can be biased compared to the intrinsic PDF, as shown in Fig. 21.

Finally, in Fig. 22, we summarize how the mean polarization fraction changes with increasing beam sizes at 1.5 and at 6.5 GHz. We show the mean polarization of the ∼60 kpc downstream region with and without the RM contribution (see Section 4.3). For the redshift considered here ($z = 0.22$) we measure a significant drop of polarization for beam resolutions below 2 arcsec. This gradual decline will clearly depend not only on the size of the beam, but also on the underlying turbulent medium. The 2L/3 case decreases from ∼50 per cent to ∼40 per cent at 1.5 GHz and from ∼65 per cent to ∼45 per cent at 6.5 GHz. On the other hand, the L/4 case decreases from ∼40 per cent to ∼30 per cent at 1.5 GHz and from ∼50 per cent to ∼25 per cent at 6.5 GHz. These differences between both models
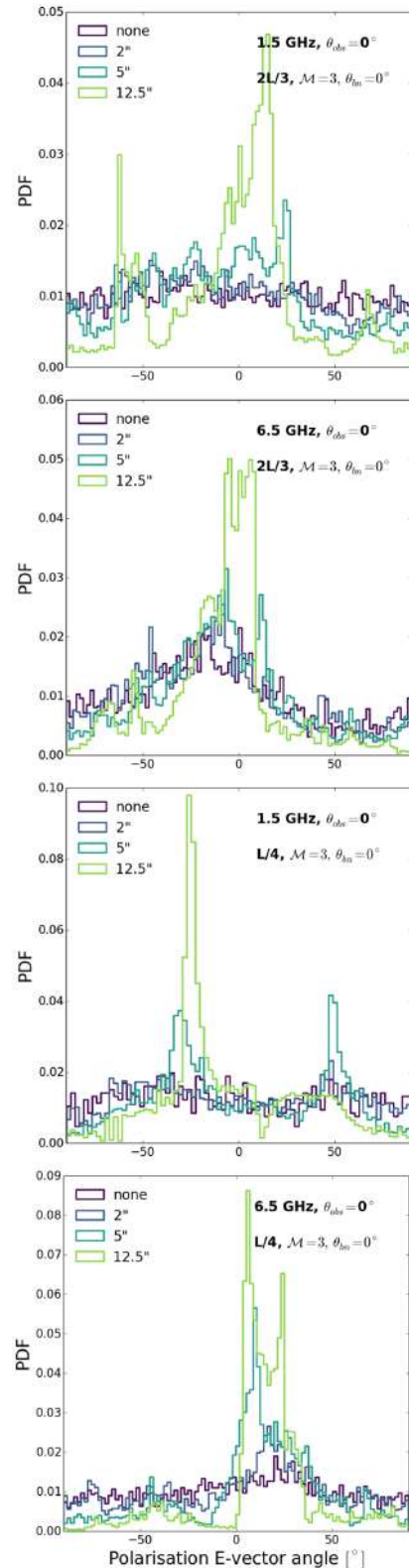
Figure 21. PDFs of the polarization E-vector angles considering $\theta_{obs} = 0°$ at different frequencies and different beam sizes (see Table 3). The two upper panels show the $2L/3$, $\mathcal{M} = 3$, and $\theta_{bn} = 0°$ case, and the two lower panels show the $L/4$, $\mathcal{M} = 3$, and $\theta_{bn} = 0°$ case. The first (second) and third (fourth) panels correspond to 1.5 GHz (6.5 GHz).
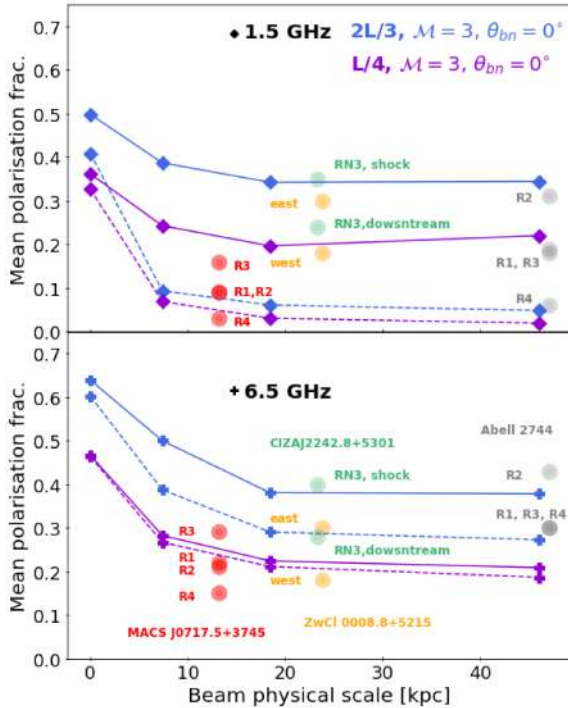
Figure 22. Mean polarization fraction at 1.5 GHz (*upper panel*) and 6.5 GHz (*lower panel*) of the of ∼60 kpc downstream region versus resolution (see Table 3) for our two models. We show the mean polarization fraction without the contribution of RM (*solid lines*) and with the RM contribution (*dashed lines*). We overplot data from the regions of the relic: MACS J0717.5+3745 [red: 1.5 GHz (*upper panel*) and 5.5 GHz (*lower panel*); Rajpurohit et al. 2021b], Abell 2744 [grey: 1.5 GHz (*upper panel*; Rajpurohit et al. 2021b) and 2–4 GHz (lower panel; R1 from Rajpurohit et al. 2021b and R2, R3, and R4 from Pearce et al. 2017)], ZwCl 0008.8+5215 [orange: 2–4 GHz (same data in both panels); Golovich et al. 2017], and CIZAJ2242.8+5301 [green: 1.5 GHz average values at the shock location and at the downstream (*upper panel*) and best-fitting average values at the corresponding regions (*lower panel*); Di Gennaro et al. 2021].

are tightly related to (1) the amount of compression at the shock front and (2) how the B_x–B_y distribution becomes more isotropic towards the downstream (see discussion in Section 4.2).

The effect of beam depolarization becomes more significant if we consider internal Faraday rotation (see dashed lines in Fig. 22). At 1.5 GHz, the mean polarization fraction of both models can decrease to ≲ 1 per cent at the lowest resolution. At 6.5 GHz, the mean polarization fraction can drop to ∼20–30 per cent. In this case, the effect of Faraday rotation is smaller and as a consequence the decrease is more subtle. The 2L/3 case suffers of more Faraday depolarization than the L/4 case due to the larger RM values (see Section 4.3). This aggravates the depolarization at lower resolution in the 2L/3 case.

We compare these values with data from three relics that can qualitatively be compared to our work:

(1) The relic in MACS J0717.5+3745 (see van Weeren et al. 2017; Bonafede et al. 2018; Rajpurohit et al. 2021a) with a Mach number of $\mathcal{M} = 3.3$, as inferred from the injection spectral index α_{int} in Rajpurohit et al. (2021a), exhibits polarization intensity values in the *VLA* L-band at 1–2 GHz of 0.01–0.06 mJy per beam with a resolution of 5 arcsec (e.g. Bonafede et al. 2009b; Rajpurohit et al. 2021b). The authors observe that the polarization fraction increases with increasing angular resolution, which is in agreement with our

results. The low mean polarization fraction observed in the relic can plausibly be explained by a turbulent ICM if internal Faraday rotation is included in the polarization computation. We can see that the observation values at 1.5 GHz for all regions of the relic and specially for regions R1 and R2 lie within the expectations of both turbulent models (see upper panel of Fig. 22). At 6.5 GHz, the L/4 case seems to be favoured (see lower panel of Fig. 22). However, the observational values reported in the lower panel of the figure are obtained at 5.5 GHz, in which case we would expect a slightly lower mean polarization in our data points.

(2) The polarized relics observed in Abell 2744 at $z = 0.308$ (Pearce et al. 2017) with Mach numbers ranging from $\mathcal{M} \sim 2$ (R2, R3, and R4) to $\mathcal{M} \sim 3$ (R1; see also Paul et al. 2019). At 2–4 GHz and a resolution of 10 arcsec, R1 shows a polarization fractions ∼52 per cent locally and ∼27 per cent globally. When we compare these observational values to our models at 1.5 GHz, we note that only the results with internal Faraday rotation are in line with the observed mean polarization fraction in R4, whereas R1, R2, and R3, are in line with the results without internal Faraday rotation. On the other hand, the relics R1, R3, and R4 have a mean polarization fraction that lies within the results of the 2L/3 model with Faraday rotation at 6.5 GHz. Yet, if the data is observed at lower frequencies, i.e. 2–4 GHz, this suggests that the two turbulent models presented in this work yield too low values to explain the mean polarization fraction in Abell 2744. We note that the observational data showed in the lower panel from Pearce et al. 2017 is not corrected by the effect of Faraday rotation, so these values may change. As of yet, our results suggest that the majority of relics in Abell 2744 may be better explained by a magnetic configuration with larger characteristic scales than our 2L/3 model and/or with a lower magnetic field strength such that the effect of internal Faraday depolarization is reduced.

(3) The relics in the cluster ZwCl 0008.8+5215 at $z = 0.104$ (see Golovich et al. 2017) with Mach numbers ranging from $\mathcal{M} = 2.2$ (eastern relic) to $\mathcal{M} = 2.4$ (western relic) have polarization fractions of ∼30 per cent and ∼18 per cent, respectively, at 2-4 GHz and a resolution of 12 arcsec. The comparison of these observational values to both our turbulent models entails very similar conclusions to those for R1, R2, and R3 in Abell 2744. The eastern relic's alignment of the polarization *E*-vectors and the level of polarization suggests that this relic could also be an outcome of a mild shock propagating through a turbulent ICM only in the case where the magnetic field is coherent in larger scales than that of our 2L/3 model.

(4) The northern relic in the galaxy cluster CIZAJ2242.8+5301 at $z = 0.1921$ (van Weeren et al. 2010, 2011b) with a Mach number of $\mathcal{M} = 2.58$, as inferred from the injection spectral index in Di Gennaro et al. (2018). Recently, Di Gennaro et al. (2021) did a high-resolution study of the polarization properties of this relic. The authors report RM values ranging from ∼−150 to ∼130 rad m^{-2}. The intrinsic polarization fraction 7 arcsec resolution maps at 1.5 GHz reveal values of up to ∼60 per cent and down to ∼20 per cent. Comparing with our mean intrinsic polarization values at 1.5 GHz (solid lines in Fig. 22), we see that the values fall in the expectations for both turbulent models. The observational mean values are reported at the shock front and the downstream, so we expect the mean value of both regions to be in between the former two. This favours no particular model at 1.5 GHz. Nevertheless, we would expect those values to be slightly higher at 6.5 GHz. In this case, the 2L/3 model would be favoured. Overall, the variations in the polarization fraction together with the first-time observed depolarization towards the downstream makes this relic a clear example of a mild shock propagating through a turbulent ICM.

5 SUMMARY AND CONCLUSIONS

Radio relics have a high polarization fraction, up to 65 per cent (e.g. van Weeren et al. 2010, 2012; Owen et al. 2014; Kierdorf et al. 2017; Loi et al. 2020; Rajpurohit et al. 2020b), with the electric field vector often aligned with the shock normal (e.g. van Weeren et al. 2010; Golovich et al. 2017; Pearce et al. 2017). The cause of the high polarization fraction and of the alignment of the magnetic field with the shock surface remain unclear. Possible causes could be large-scale, uniform fields, or compression of a randomly orientated magnetic field (e.g. Laing 1980). However, some radio relics show more complex polarization patterns. In particular, some observed radio relics show high polarization fractions at the shock front contrary to theoretical expectations (e.g. Rajpurohit et al. 2020b, 2021b; Di Gennaro et al. 2021).

We have studied the intrinsic polarized emission from a shock wave propagating through a medium perturbed by decaying subsonic turbulence in the ICM. In our hybrid simulations, the MHD grid represents a thermal fluid, whereas Lagrangian particles represent CR electrons. We injected CR electrons at the shock assuming diffusive shock acceleration, after which each CR electron evolves at run-time according to a cosmic ray transport equation including adiabatic, synchrotron, and inverse Compton losses.

We explored shocks with $\mathcal{M} = 3$, typical of merger shock waves. We varied the downstream turbulence using turbulence-in-a-box simulations as previously considered in Paper I; solenoidal subsonic turbulence with power peaking at 133 kpc ($2L/3$ case) and solenoidal subsonic turbulence with power peaking at 50 kpc ($L/4$ case). One snapshot of each simulation was selected as an initial condition for our subsequent shock simulation. We also varied the observing angles, beam sizes, and observing frequencies. Our most important results can be summarized as follows:

(i) *Intrinsic polarization fraction*: The morphology of polarized emission resembles the structures of the underlying turbulent ICM. In particular, we observe a high polarization fraction at the shock front, which decreases in the downstream region. We find that the degree of anisotropy in the downstream magnetic configuration defines the amount of depolarization behind the shock. Since this trend is also observed in some of the best-studied relics such as the Sausage relic (e.g. Di Gennaro et al. 2021) or that in the MACSJ0717.5+3745 galaxy cluster (e.g. Rajpurohit et al. 2021b), this confirms that polarized radio relics can also be formed in a tangled magnetic field. On the other hand, we showed that in a uniform ICM the polarization fraction increases downstream, at odds with observations.

(ii) *Alignment of the intrinsic polarization E-vectors*: We found that a high degree of alignment at the shock front can also be reproduced in a turbulent environment. In particular, we find that the distribution of polarization E-vector angles strongly depends on the upstream properties leading to differences between the two turbulent models studied. We conclude that these differences between models are likely to be an outcome of the amount of amplification of $B_\perp$ which indirectly depends on the properties of the turbulent media such as the characteristic magnetic field scale λ_B among others. This alignment, together with variations in the polarization fraction in the downstream regions, is observed too for example in the Sausage relic (e.g. Di Gennaro et al. 2021).

(iv) *Internal Faraday rotation*: Our results suggest that at 6.5 GHz, the effect of Faraday depolarization is marginal leaving the intrinsic trends unaffected (see point i). On the other hand, already at 1.5 GHz we find different degrees of Faraday depolarization depending on the upstream turbulent configuration. Finally, Faraday depolarization becomes significant at 150 MHz. Our 2L/3 model leads to a non-Gaussian RM distribution similarly to what has also been observed in cosmological simulations (e.g. Wittor et al. 2019). We caution that non-Gaussianity could result in discrepancies with respect to the common assumptions of symmetric RM distributions (e.g. Burn 1966; Tribble 1991; Sokoloff et al. 1998).

(v) *Beam depolarization*: Our study shows that Gaussian convolution for the limited beam size strongly affects the polarization fraction and orientation of the polarization E-vectors in a turbulent ICM. In particular, we observe the effect of beam depolarization when going to lower resolutions. For example, the mean polarization fraction can drop down to ∼10–30 per cent at a resolution of 12.5 arcsec, depending on the turbulent model and the observing frequency. We find that the orientation of the polarization E-vectors is mainly affected at the downstream of the shock. We find that the distribution of polarization angles at a resolution of 12.5 arcsec tends to narrow down. As a consequence, the polarization E-vectors may appear to be aligned even if the underlying medium is turbulent.

In summary, we have identified key features that are likely to affect also the polarized emission from radio relics forming in a turbulent ICM. Our work confirms that a shocked turbulent ICM can reproduce the observed polarization fraction from the shock surface, in contrast to a uniform ICM. We find that the degree of alignment of the E-vectors with the shock normal also depends on the level of underlying turbulence, and that a high alignment of the polarization E-vectors at the very shock front, as observed in most of the radio relics, can be found in a turbulent medium. We expect higher Mach number shocks to produce higher polarization fractions at the shock front. Yet, the observed polarization in relics would be hard to reproduce with $\mathcal{M} \sim 2$ due to the low level of compression (see also Paper I). We compared our results to the mean polarization fraction observed in some relics such as those in the galaxy clusters MACS J0717.5+3745, CIZAJ2242.8+5301, Abell 2744, and ZwCl 0008.8+5215, and found that a turbulent ICM can reproduce comparable values in some cases. At the same time, our results highlight the complexity of reproducing one-to-one relations with observations, and of generalizing the upstream characteristics to all relics. Indeed, there is substantial diversity of radio relics depending on the individual merger history of each galaxy cluster as well as on the viewing angle. In future work, we plan to tackle this issue by studying different viewing angles in combination with a broader range of initial turbulent ICM conditions considering different rms Mach numbers, magnetic field strengths, injection scales, and types of forcing.

DATA AVAILABILITY STATEMENT

The data underlying this article will be shared on reasonable request to the corresponding author.

REFERENCES

Aghanim N. et al., 2020, A&A, 641, A6
Anderson C. S., Gaensler B. M., Heald G. H., O'Sullivan S. P., Kaczmarek J. F., Feain I. J., 2018, ApJ, 855, 41
Blandford R., Eichler D., 1987, Phys. Rep., 154, 1
Böhringer H., Chon G., Kronberg P. P., 2016, A&A, 596, A22
Bonafede A., Giovannini G., Feretti L., Govoni F., Murgia M., 2009a, A&A, 494, 429
Bonafede A. et al., 2009b, A&A, 503, 707
Bonafede A. et al., 2012, MNRAS, 426, 40
Bonafede A., Vazza F., Brüggen M., Murgia M., Govoni F., Feretti L., Giovannini G., Ogrean G., 2013, MNRAS, 433, 3208
Bonafede A. et al., 2018, MNRAS, 478, 2927
Botteon A., Brunetti G., Ryu D., Roh S., 2020a, A&A, 634, A64
Botteon A. et al., 2020b, ApJ, 897, 93
Brentjens M. A., 2008, A&A, 489, 69
Brentjens M. A., de Bruyn A. G., 2005, A&A, 441, 1217
Brüggen M., Bykov A., Ryu D., Röttgering H., 2012, Space Sci. Rev., 166, 187
Brüggen M., Vazza F., 2020, MNRAS, 493, 2306
Burn B. J., 1966, MNRAS, 133, 67
Bykov A. M., Kaastra J. S., Brüggen M., Markevitch M., Falanga M., Paerels F. B. S., 2019, Space Sci. Rev., 215, 27
Calder A. C. et al., 2002, ApJS, 143, 201
Caprioli D., Spitkovsky A., 2014a, ApJ, 783, 91
Caprioli D., Spitkovsky A., 2014b, ApJ, 794, 46
Childs H. et al., 2012, in High Performance Visualization–Enabling Extreme-Scale Scientific Insight. Chapman and Hall/CRC, Boca Raton, FL, p. 357
Clarke T. E., Ensslin T. A., 2006, AJ, 131, 2900
de Gasperin F., van Weeren R. J., Brüggen M., Vazza F., Bonafede A., Intema H. T., 2014, MNRAS, 444, 3130
de Gasperin F., Intema H. T., van Weeren R. J., Dawson W. A., Golovich N., Wittman D., Bonafede A., Brüggen M., 2015, MNRAS, 453, 3483
Dedner A., Kemm F., Kröner D., Munz C. D., Schnitzer T., Wesenberg M., 2002, J. Comput. Phys., 175, 645
Di Gennaro G. et al., 2018, ApJ, 865, 24
Di Gennaro G. et al., 2021, ApJ, 911, 21
Domínguez-Fernández P., Brüggen M., Vazza F., Banda-Barragán W. E., Rajpurohit K., Mignone A., Mukherjee D., Vaidya B., 2021, MNRAS, 500, 795 (Paper I)
Drury L. O., 1983, Re. Prog. Phys., 46, 973
Engel A. R., 1979, Phys. Bull., 30, 158
Ensslin T. A., Biermann P. L., Klein U., Kohle S., 1998, A&A, 332, 395
Fryxell B. et al., 2000, ApJS, 131, 273
Ginzburg V. L., Syrovatskii S. I., 1965, ARA&A, 3, 297
Golovich N., van Weeren R. J., Dawson W. A., Jee M. J., Wittman D., 2017, ApJ, 838, 110
Guo X., Sironi L., Narayan R., 2014, ApJ, 797, 47
Hoeft M., Brüggen M., 2007, MNRAS, 375, 77
Hong S. E., Kang H., Ryu D., 2015, ApJ, 812, 49
Hutschenreuter S., Enßlin T. A., 2020, A&A, 633, A150
Johnston-Hollitt M., Ekers R. D., 2004, preprint (arXiv:astro-ph/0411045)
Kale R., Dwarakanath K. S., Bagchi J., Paul S., 2012, MNRAS, 426, 1204
Kang H., Ryu D., Jones T. W., 2012, ApJ, 756, 97
Kang H., Ryu D., Ha J.-H., 2019, ApJ, 876, 79

Kierdorf M., Beck R., Hoeft M., Klein U., van Weeren R. J., Forman W. R., Jones C., 2017, A&A, 600, A18
Klein U., Fletcher A., 2015, Galactic and Intergalactic Magnetic Fields. Springer Praxis Books, Springer International Publishing
Laing R. A., 1980, MNRAS, 193, 439
Landau L. D., Lifshitz E. M., 1987, in Landau L. D., Lifshitz E. M., eds, Fluid Mechanics, 2nd edn., Vol. 6, Course of Theoretical Physics. Butterworth-Heinemann, Oxford
Lerato Sebokolodi M., Perley R., Eilek J., Carilli C., Smirnov O., Laing R., Greisen E., Wise M., 2020, preprint (arXiv:2009.06554)
Locatelli N. T. et al., 2020, MNRAS, 496, L48
Loi F. et al., 2020, MNRAS, 498, 1628
Lyutikov M., Pariev V. I., Blandford R. D., 2003, ApJ, 597, 998
Malkov M. A., Drury L. O., 2001, Rep. Prog. Phys., 64, 429
Mignone A., Bodo G., Massaglia S., Matsakos T., Tesileanu O., Zanni C., Ferrari A., 2007, ApJS, 170, 228
Miyoshi T., Kusano K., 2005, J. Comput. Phys., 208, 315
Nuza S. E., Gelszinnis J., Hoeft M., Yepes G., 2017, MNRAS, 470, 240
Owen F. N., Rudnick L., Eilek J., Rau U., Bhatnagar S., Kogan L., 2014, ApJ, 794, 24
Ozawa T. et al., 2015, PASJ, 67, 110
Park J., Caprioli D., Spitkovsky A., 2015, Phys. Rev. Lett., 114, 085003
Paul S., Salunkhe S., Datta A., Intema H. T., 2019, MNRAS, 489, 446
Pearce C. J. J. et al., 2017, ApJ, 845, 81
Pinzke A., Oh S. P., Pfrommer C., 2013, MNRAS, 435, 1061
Pizzo R. F., de Bruyn A. G., Bernardi G., Brentjens M. A., 2011, A&A, 525, A104
Purcell C. R., Van Eck C. L., West J., Sun X. H., Gaensler B. M., 2020, RM-Tools: Rotation Measure (RM) Synthesis and Stokes QU-fitting. Astrophysics Source Code Library, record ascl:2005.003
Rajpurohit K. et al., 2018, ApJ, 852, 65
Rajpurohit K. et al., 2020a, A&A, 636, A30
Rajpurohit K. et al., 2020b, A&A, 642, L13
Rajpurohit K. et al., 2021a, A&A, 646, A56
Rajpurohit K. et al., 2021b, preprint (arXiv:2104.05690)
Rybicki G. B., Lightman A. P., 1979, Radiative Processes in Astrophysics. Wiley Online Library, Weinheim
Ryu D., Kang H., Ha J.-H., 2019, ApJ, 883, 60
Sahni V., Sathyaprakash B. S., Shandarin S. F., 1998, ApJ, 495, L5
Schmalzing J., Buchert T., 1997, ApJ, 482, L1
Schmalzing J., Buchert T., Melott A. L., Sahni V., Sathyaprakash B. S., Shandarin S. F., 1999, ApJ, 526, 568
Skillman S. W., Xu H., Hallman E. J., O'Shea B. W., Burns J. O., Li H., Collins D. C., Norman M. L., 2013, ApJ, 765, 21
Sokoloff D. D., Bykov A. A., Shukurov A., Berkhuijsen E. M., Beck R., Poezd A. D., 1998, MNRAS, 299, 189
Stuardi C. et al., 2019, MNRAS, 489, 3905
Tribble P. C., 1991, MNRAS, 253, 147
Vaidya B., Mignone A., Bodo G., Rossi P., Massaglia S., 2018, ApJ, 865, 144
van Haarlem M. P. et al., 2013, A&A, 556, A2
van Weeren R. J., Röttgering H. J. A., Brüggen M., Hoeft M., 2010, Science, 330, 347
van Weeren R. J., Brüggen M., Röttgering H. J. A., Hoeft M., 2011a, JA&A, 32, 505
van Weeren R. J., Brüggen M., Röttgering H. J. A., Hoeft M., 2011b, MNRAS, 418, 230
van Weeren R. J., Hoeft M., Röttgering H. J. A., Brüggen M., Intema H. T., van Velzen S., 2011c, A&A, 528, A38
van Weeren R. J., Röttgering H. J. A., Intema H. T., Rudnick L., Brüggen M., Hoeft M., Oonk J. B. R., 2012, A&A, 546, A124
van Weeren R. J. et al., 2017, ApJ, 835, 197
van Weeren R. J., de Gasperin F., Akamatsu H., Brüggen M., Feretti L., Kang H., Stroe A., Zandanel F., 2019, Space Sci. Rev., 215, 16
Vazza F., Brüggen M., Hinz P. M., Wittor D., Locatelli N., Gheller C., 2018, MNRAS, 480, 3907
Wittor D., Hoeft M., Vazza F., Brüggen M., Domínguez-Fernández P., 2019, MNRAS, 490, 3987
ZuHone J. A., Markevitch M., Weinberger R., Nulsen P., Ehlert K., 2020, BAAS, 52, 1

APPENDIX A: BEAM EFFECTS IN THE UNIFORM MEDIUM

In Fig. A1 we show the maps of the polarization fraction and the corresponding polarization E-vectors, in a uniform media with different magnetic orientations (see Table 1). This figure shows the same configuration as Fig. 4, i.e. considering and observing angle of $\theta_{obs} = 0°$ and 150 MHz. The polarization fraction maps are smoothed with a Gaussian kernel, considering the same three beam sizes as in Section 4.4. We observe that the gradient of polarization fraction, spanning from ∼0.7 to ∼0.8 in both magnetic field orientations, remains unchanged as in Fig. 4. Moreover, in a uniform medium the alignment of the polarization E-vectors remains unchanged even at lower resolution. The main effect of taking into account different beam sizes in an uniform medium, is the apparent extension of the downstream region. In particular, the shock front region with a low polarization fraction of ∼0.7 and an extension of ≲ 20 kpc (purple region) can appear to be twice as large for the 12.5 arcsec × 12.5 arcsec beam size. As we suggested in the analysis of the turbulent medium, and as expected, a resolution higher than 5 arcsec × 5 arcsec would more accurately reproduce the maps of polarization fraction.
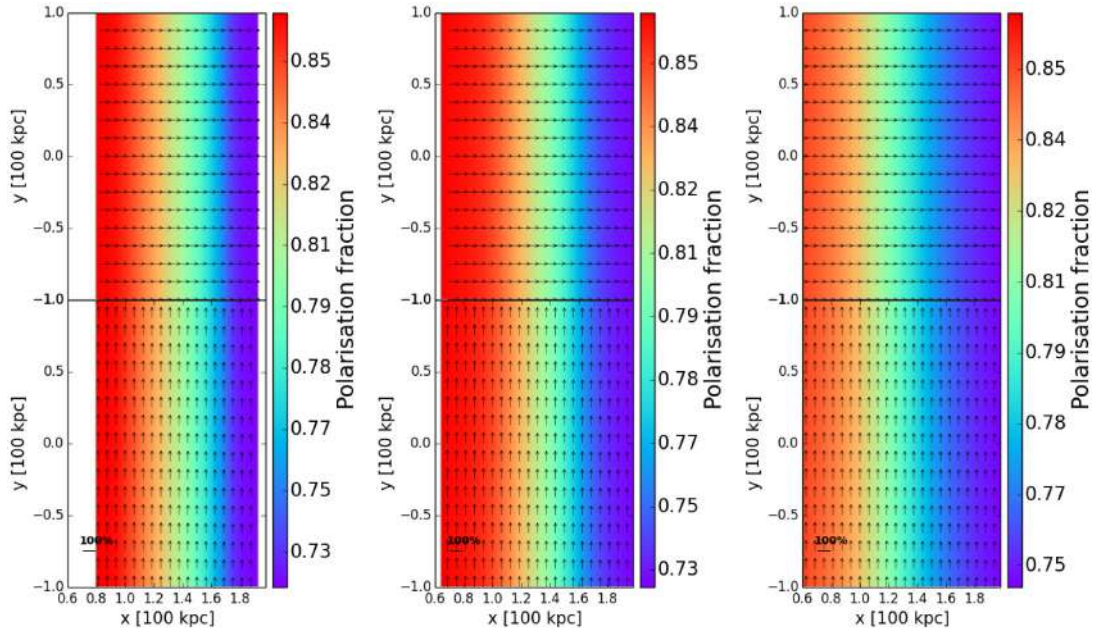
Figure A1. Smoothed polarization fraction maps of the uniform medium considering $\theta_{obs} = 0°$ at 150 MHz. We show the two magnetic field orientations: in the y-direction (*upper panels*) and the x-direction (*lower panel*). The first, second, and third columns correspond to beam sizes of 2 arcsec × 2 arcsec, 5 arcsec × 5 arcsec and 12.5 arcsec × 12.5 arcsec, respectively. We overplot the polarization E-vectors.

This paper has been typeset from a T$_{\text{E}}$X/L$^{\text{A}}$T$_{\text{E}}$X file prepared by the author.